What steers the “folding to faulting” transition in carbonate-dominated seismic fold-and-thrust belts? New insights from the Eastern Southern Alps (Northern Italy)

What steers the "folding to faulting" transition in carbonate-dominated seismic fold-and-thrust belts? New insights from the Eastern Southern Alps (Northern Italy)

Zuccari C.[1](*), Viola G.[1], Curzi M.[1], Aldega L.[2] and Vignaroli G.[1]

[1] Alma Mater Studiorum, University of Bologna, Department of Biological, Geological and Environmental Sciences - BiGeA, Bologna, Italy.

[2] Sapienza, University of Rome, Department of Earth Sciences, Rome, Italy.

***Corresponding author:**

Costantino Zuccari

Dipartimento di Scienze Biologiche, Geologiche e Ambientali
Alma Mater Studiorum – Università degli Studi di Bologna
Via Zamboni, 67 – 40126 Bologna (Italy)
costantino.zuccari2@unibo.it
+393398768039

Abstract

Several parameters steer the modes of shortening of carbonate-dominated fold-and-thrust belts from incipient- (layer parallel shortening, buckle folds) to evolved deformation stages (verging folds, discrete thrusts). In this study, we address the spatial and temporal evolution of compressive structures within carbonate-dominated fold-and-thrust belts by documenting the geometry, kinematics and structural architecture of the San Donato-Costa Thrust Zone, a splay of the regional Belluno Thrust of the seismically active Eastern Southern Alps (Northern Italy). Deformation is there accommodated by a variety of features ranging from open and upright to tight and verging folds cut by later thrusts. An integrated structural analysis indicates inherited primary features to have effectively steered the deformation style of the thrust and its immediate hanging wall and footwall. We propose an evolving deformation scenario initially governed by the inherited lithological features and localised pressure-solution, then by the geometry of folds accommodating progressive shortening and, finally, by thrusting. The folding-faulting transition occurs when forelimbs dip ~ 80° and the ratio between the dip angle of fore- and back limbs is ~ 3.3. These geometric boundary conditions control the mechanical behaviour of carbonate multilayer successions during orogenic shortening in fold-and-thrust belts, assisting the partitioning between seismic and aseismic deformation.

Keywords: Eastern Southern Alps; Folding-faulting transition; Carbonate multilayers; Mechanical stratigraphy; Seismic behaviour; Seismic vs. aseismic.

1. Introduction

Deformation in carbonate rocks in any given geodynamic setting is steered and modulated by a broad spectrum of boundary conditions. Among others, i) rock type and mechanical stratigraphy, ii) pressure and temperature, iii) stress field orientation, iv) presence and composition of fluids, v) presence and spatial distribution of inherited sedimentary and structural anisotropies, such as bedding, foliation planes and inherited faults, seem to play a key role in governing the deformation style both in compressive and in extensional settings (Stewart and Hancock, 1991; Bigi et al., 2003; Billi et al., 2003; Billi, 2010; Labaume et al., 2004; Collettini et al., 2009; Cilona et al., 2012; Fagereng et al., 2014; Michie et al., 2014; Bussolotto et al., 2015; Ikari et al., 2015; Tavani et al., 2015; Delle Piane et al., 2017).

In carbonate-dominated fold-and-thrust belts folding and thrusting can coexist to accommodate deformation at all scales. Folding is commonly associated with aseismic creep whereas thrusting occurs mainly by cyclic seismic rupturing (e.g., Erickson, 1996; Ruh et al., 2012; Swanson et al., 2012; Tesei et al., 2013; Tavani et al., 2015; Bigi et al., 2018; Curzi et al., 2020). Also, the compositional heterogeneity of carbonates, which is due to inherently different marl/limestone ratios and to the primary porosity, plays a significant role in the localisation of deformation during both diffuse folding (Ramsay and Graham, 1970; Fischer and Jackson, 1990; Micarelli et al., 2006; Tondi et al., 2006; Dautriat et al., 2011; Cilona et al., 2012, 2014; Lena et al., 2015; Nabavi and Fossen, 2021) and discrete (seismic) thrusting (Tavani et al., 2008; Smith et al., 2011; Collettini et al., 2013; Bullock et al., 2014; Michie, 2015; Giorgetti et al., 2016). Understanding the evolution of folding and faulting and their mutual relationships in space and through time is, thus, key to the unravelling and constraining of progressive deformation histories and seismogenesis of carbonate-dominated fold-and-thrust belts (Ramsay, 1974; Tavarnelli, 1997; Simpson, 2009; Hudleston and Treagus, 2010; Kilian et al., 2011; Tavani et al., 2015; Tavarnelli et al., 2021).

It is widely documented that the transition from upright and symmetric buckle folds to more mature, tight to asymmetric folds occurs in response to the progressive accommodation of distributed deformation (Hudleston et al., 1996; Butler et al., 2020; Humair et al., 2020). Faulting, on the other hand, is the result of deformation localisation associated with the progressive increase of shortening, as documented by numerical models and field studies (e.g., Lacombe et al., 2007; Simpson, 2009; Humair et al., 2020; Kilian et al., 2021). In particular, faulting in a progressively developing fold-and-thrust belt occurs when folds reach their lock-up stage such that no further shortening can be accommodated by their continued tightening and amplification (e.g., Ramsay, 1974; Fischer et al., 1992; Simpson, 2009; Butler et al., 2019). Two crucial issues regarding the folding-faulting transition are, however, still poorly addressed and, thus, understood:

(i) is there a given quantifiable deformation threshold beyond which folding gives way to faulting?

(ii) (ii) which parameters steer this transition and the switch of deformation mechanisms in carbonate multilayer successions? (e.g., Marques, 2008; Simpson, 2009; Hudleston and Treagus, 2010; Humair et al., 2020).

Addressing these issues is important not only to the understanding of the geometrical, kinematic, mechanical and rheological behaviour of carbonate-dominated fold-and-thrust belts, but also to the characterisation of first-order mechanisms of deformation and strain localisation at all scales and of seismogenesis at large, the study of which commonly relies upon only indirect constraints (e.g., seismic imaging, V_p/V_s and tomographic analysis, geodetic velocity analysis; e.g., Chiarabba et al., 2005; Carminati et al., 2007; Anselmi et al., 2011; Serpelloni et al., 2016; Anderlini et al., 2020).

To help bridge this knowledge gap, here we document the geometry, kinematics and structural architecture of the San Donato-Costa Thrust Zone, a splay of the regional Belluno Thrust (Zuccari et al., 2021), which deforms a multilayer carbonate succession of the seismically active central Eastern Southern Alps of Northern Italy (Mw > 6.0 earthquakes; Galadini et al., 2005; Carminati et al., 2007;

Anselmi et al., 2011; Serpelloni et al., 2016; Anderlini et al., 2020). Based on the systematic analysis of well-preserved structures that are representative of both the local early contractional phase (i.e., the first discrete increments of shortening of the Eastern Southern Alps) by distributed folding and of later thrusts, we document and constrain the transition from folding to thrusting during progressive deformation. We show that the folding-faulting transition is governed by the progressive growth and tightening of asymmetric folds leading first to the progressive increase of the dip angle of their forelimbs and, finally, to discrete rupturing and thrusting. For the first time, we propose a numerical threshold for this transition based on the geometrical characteristics of the folded multilayer sequence, and we discuss this in the framework of the overall mechanical/seismic behaviour of fold-and-thrust belts.

2. Geological setting

2.1 The Eastern Southern Alps

The Eastern Southern Alps (hereafter ESA) are a fold-and-thrust-belt of the south-verging retro-belt of the European Alps (Fig. 1a and b), which developed during the Cretaceous-to-Neogene convergence between Europe and Adria (e.g., Doglioni and Carminati, 2008). The ESA have been shaped by several tectonic events including:

i) E-W crustal extension during the Permo-Triassic rifting leading to the development of N-S trending and orogen-scale faults and significant calcalkaline volcanism (Winterer and Bosellini, 1981; Doglioni, 1987; Bosellini et al., 2003; Schaltegger and Brack, 2007);

ii) Middle Triassic differential subsidence and local uplift, climaxing into a magmatic event during Late Ladinian times (e.g., Castellarin et al., 1988; Bosellini et al., 2003; Lustrino et al., 2019; De Min et al., 2020);

iii) Rifting starting in the Late Triassic and climaxing during the Early Jurassic (e.g., Bosellini et al., 2003; Handy et al., 2010);

iv) Cenozoic-Alpine compression, which began during the Cenozoic Europe-Adria convergence and continental collision and which is still active (Doglioni, 1987; Castellarin and Cantelli, 2000; Carminati et al., 2004; Schmid et al., 2004; Castellarin et al., 2006; D'Ambrogi and Doglioni, 2008).

These tectonic phases are well recorded within the local ESA sedimentary succession that rests upon igneous and metamorphic basement rocks of Palaeozoic age (Fig. 1b and c). This > 3 km thick sedimentary cover is made up of Permian - Lower Triassic siliciclastic units, overlain by Middle Triassic - Lower Jurassic shallow-water carbonates (Fig. 1c; Bosellini et al., 1981; Trevisani, 1991; Masetti et al., 1998). The succession ends at the top with Lower Jurassic-Neogene cherty pelagites and hemipelagites capped by Palaeocene-to-Miocene terrigenous and bioclastic formations (Fig. 1b, c; D'Alberto et al., 1995; Stefani et al., 2007).

The still ongoing Alpine compression that ensued during the Cenozoic has been and is being accommodated by south-verging thrusts and associated folds (Doglioni, 1992; Castellarin and Cantelli, 2000) and ~ 30 km of cumulative shortening is estimated across the ESA (e.g., Doglioni, 1992). From the late Tortonian to the early-Middle Pleistocene, shortening was accompanied by repeated fluctuations of the principal stress directions (from NNW-SSE to NW-SE; Caputo et al., 2010). Most crustal shortening, however, had already occurred during the late Oligocene (e.g., Doglioni, 1992; Castellarin and Cantelli, 2000; Castellarin et al., 2006) and localised along six main thrusts that formed in sequence from north to south: Valsugana, Belluno, Moline, Tezze, Bassano-Maniago and the Montello thrusts (Doglioni, 1990; Doglioni and Carminati, 2008; Fig. 1b and c). The Belluno Thrust (hereafter BT) is the focus of our study. It exhibits a ramp-flat geometry and forms a ~ 20 km long WSW-ENE-striking and ~ 30° N-dipping thrust (Fig. 1b-d) that accommodated a total shortening of ~ 6-8 km (Selli, 1998; D'Ambrogi and Doglioni, 2008). Multiple tectonic and

167 seismogenic reactivations characterised the mechanical behaviour of the BT during significant strain
168 localisation in carbonate-dominated rocks (Vignaroli et al., 2020). In the hanging wall of the BT, a
169 regional-scale anticline deforming Jurassic-Lower Cretaceous units is characterised by a sub-vertical
170 to overturned forelimb and a ~ 20° N-dipping back limb subparallel to the BT slip plane (Figs. 1b, c,
171 and 2). In the footwall there occurs the San Donato-Costa Thrust Zone (hereafter SCTZ), a second-
172 order splay of the BT, which cuts across an Upper Jurassic-lower Eocene sedimentary succession
173 (Zuccari et al., 2021; Fig. 1d).

174 From a seismotectonic perspective, the ESA are characterised by still active seismic
175 contractional deformation, as documented by recent and historical seismicity (Fig. 1a and d;
176 Serpelloni et al., 2016; Carminati et al., 2007; Anderlini et al., 2020). The available seismological
177 dataset shows that seismicity mostly localises within the ESA southernmost edge and its Triassic-to-
178 Paleogene carbonate succession along the transition to the Venetian Plain (Bassano–Maniago Thrust
179 and Montello Thrust, Fig. 1), with events up to Mw ≥ 6, as documented by a historical record spanning
180 > 1000 years (Galadini et al., 2005; Cheloni et al., 2014; Serpelloni et al., 2016).

181

182 **3. Methods**

183 Our work focuses on the folded and faulted carbonate succession in the footwall of the BT,
184 along and across the SCTZ. We integrated detailed field structural mapping and mesoscale structural
185 analysis with XRD diffraction of 17 samples collected along the studied San Donato-Costa section
186 (Fig. 3a and b). The exposed sedimentary succession was mapped at the 1:2,500 and 1:5,000 scale
187 (Zuccari et al., 2021) and further characterised from a paleontological and lithological perspective to
188 constrain its multilayer character with alternating “pure” and cherty limestone, marly-limestone and
189 marl (Fig. 3c).

A detailed field structural analysis was carried out along N-S oriented transects (parallel to the sense of tectonic transport) to assess the deformation and structural style as a function of the distance from the SCTZ. Systematic mesoscopic structural observations aimed to define the first-order structural framework of the study area and the geometric relationships between folds and faults in the hanging wall, footwall, and the thrust zone itself. This quantitative geometrical and structural characterisation relies on the following parameters:

i) α: bedding dip angle in fold back limb;

ii) β: bedding dip angle in fold forelimb;

iii) δ: dip angle of thrust in fold back limb.

The characterisation of fold (a)symmetry is based on the length of back- and forelimbs, whereby asymmetric folds are defined by a long back limb and a short forelimb, followed by another long back limb (Twiss and Moores, 1992). We implement this approach with the concept of "fold envelope surface", defined as "*the surface tangent to the individual hinges along fold layers*", Fossen, 2016; Fig. S1). Considering a low dip angle envelope surface, an increasing length difference between back- and forelimb is also accompanied by the increase of the β/α ratio (Fig. S1). It follows that the β/α ratio can be taken as a reliable indicator of fold (a)symmetry (Fig. S1).

X-ray diffraction was performed to define mineralogical and compositional heterogeneities within the multilayer succession and allow for the assessment of the mechanical implications thereof. Ten samples were collected from limestone beds and seven from calcareous marl layers (Fig. 3a, Tables S1 and S2). We refer the readers to the Supplementary Material for detailed information on the methodology and instrumentation.

214 ## 4. Results

215 ### 4.1 Structural framework of the San Donato - Costa Thrust Zone

216 The SCTZ cuts across an up to 650 m thick carbonate multilayer succession (Figs. 1d, 2 and
217 3). From bottom to top, this succession includes: i) the Rosso Ammonitico Veronese (Bajocian *p.p.* -
218 upper Tithonian *p.p.*), which consists of massive to well-bedded nodular red and grey limestone and
219 marly limestone; ii) the Maiolica Fm. (upper Tithonian *p.p.* - lower Aptian), an up to 300 m thick
220 succession of cherty limestone with alternating 5-10 cm thick marly beds toward the top (Fig. 3b and
221 c); iii) the Scaglia Variegata Alpina Fm. (lower Aptian - lower Turonian *p.p.*), formed by a ca. 30 m
222 thick marly and clay rich lower member (Fig. 3c) and by a ~ 50 m thick more calcareous upper
223 member (Fig. 3b and c); iv) the Scaglia Rossa Fm. (lower Turonian *p.p.*- lower Eocene *p.p.*), formed
224 by a ca. 150 m thick well bedded sequence of marl and calcareous marl (Fig. 3c). The succession is
225 capped by ~ 110 m of marl and shale with rare calcareous intercalations (Marna della Vena d'Oro
226 Fm., upper Palaeocene - lower Eocene *p.p.*, Fig. 3c).

227 The SCTZ is a 2 km long, E-W-striking and SSE verging thrust defined by a main single slip
228 plane in its eastern sector, which passes into several anastomosed fault-splays in the west (Figs. 2, 3a
229 and b). The estimated stratigraphic throw along the SCTZ is up to ~ 60 m in the east, whereas it
230 progressively increases up to several hundred meters toward the west (Fig. 3a and b). The hanging
231 wall of the SCTZ is folded by a km-scale anticline (Figs. 2 and 3a) with a steep-to-subvertical S-
232 dipping forelimb made of the Maiolica Fm. (Fig. 3b). The immediate footwall of the SCTZ is formed
233 by an overturned syncline cored by the Scaglia Rossa Fm. (Figs. 2 and 3a-b). Mesoscopic parasitic
234 fold trains occur along the ~ 20° NNW-dipping back limb of the hanging wall anticline and along the
235 ~ 20° NNW-dipping forelimb of the footwall syncline (Fig. 3a and b). These parasitic folds are locally
236 cut across by top-to-the SE mesoscopic thrusts, that accommodate centimetric to metric offsets, and
237 are spatially arranged in mesoscale duplexes in the Scaglia Rossa Fm. along the syncline forelimb.

238 In the following, we illustrate the main structures of the SCTZ by taking a virtual journey from
239 the hanging wall in the north to the footwall in the south (Fig. 3).

240

241 **4.1.1 Hanging wall of the San Donato - Costa Thrust Zone**

242 The northernmost portion of the considered hanging wall section (i.e., hundreds of metres far
243 away from the SCTZ; Figs. 2 and 3) contains evidence of bedding-perpendicular pressure solution
244 within the Maiolica Fm. (Figs. 4a and 5). Pressure solution planes systematically abut against
245 bedding. This is evident within both tabular (Fig. 5a and b) and not folded domains as well as in
246 symmetric buckle folds (Fig. 5c), where pressure solution planes are invariably perpendicular to
247 bedding, irrespective of their position within the fold (Fig. 5d-f). This observation suggests that
248 pressure solution planes formed prior to folding (Fig. 5c-f). Pressure-solution planes are at a constant
249 spacing of ~ 10 cm within the same bed (Fig. 5a), although spacing tends to increase with bed
250 thickness (Fig. 5c). Traces of insoluble material are locally preserved and define the pressure solution
251 planes (Fig. 5b). The latter are generally tabular and rather smooth. Minor N-dipping thrust planes
252 dipping at ~ 35° (δ) locally exploit bed-bed interfaces (Fig. 5b) and cut across the bed-perpendicular
253 pressure solution planes (Fig. 5b). Such thrust planes are systematically found along the tabular
254 portions of the succession where they are decorated by slickenlines and slickenfibres, which
255 invariably indicate a top-to-the SE sense of shear (Fig. 5b).

256 Moving to the SCTZ, the number of folds in the hanging wall increases while their wavelength
257 decreases (Figs. 2, 3a-b, 6a). There, Maiolica limestones deformed by open and upright folds (Fig.
258 4d) lack evidence of pressure solution (Fig. 6b). Open folds have wavelengths in the 3-5 m range,
259 amplitudes up to 2 m, and symmetric shapes with comparable dip angle for both limbs (α and β =
260 32°; Figs. 4b and 6b). Farther to the south and close to the SCTZ, folds wavelength and amplitude
261 decrease to an average of ~ 90 cm and ~ 40 cm, respectively (Fig. 6c and d). Folds tend to become
262 south-verging and more asymmetric, with back limbs dipping to the NW (α = 35°) and forelimbs to

263 the SE (β = 50°; Figs. 4b and 6c). In place, folds are locally faulted by bed-parallel, top-to-the SE
264 thrusts that dip toward the NW (δ = 35°- 40°) and accommodate centimetric to metric offsets along
265 bed-bed interfaces (Fig. 6c). As one approaches the SCTZ (Fig. 3a and b, Fig. 6a), the fold wavelength
266 decreases further, and folds tend to tighten even more as part of a clear strain gradient (Fig. 6d). Their
267 wavelength and amplitude decrease and back limbs and forelimbs dip toward the NW (α = 50°- 65°)
268 and to the SE (β = 55° - 70°), respectively (Figs. 4b and 6d).

269 While the deformation structures described above deform the calcareous Maiolica Fm. along
270 the western termination of the SCTZ, in the eastern part of the hanging wall the Scaglia Rossa Fm. is
271 exposed. The deformation style therein is significantly different as it is mostly distributed (Figs. 3a
272 and 7). In particular, pervasive S-C fabrics mainly affect the steeply dipping or overturned fold limbs
273 (β = 68°- 75°). The steeply dipping fold limbs are commonly dissected by closely spaced C planes
274 (Fig. 7a, c and d). Locally, deformation is also accommodated by foliated domains within the marly
275 layers of the Scaglia Rossa Fm. (Fig. 7b), which develop along NW-dipping bed-bed interfaces. S-C
276 fabrics mostly indicate a top-to-the SE sense of shear (Fig. 7a and b) that is consistent with the
277 transport of the principal thrusts, and, only to a lesser extent, top-to-the NE shearing, probably related
278 to a reactivation during localised back thrusting (Fig. 7c).

279

280 **4.1.2 The thrust zone**

281 The actual SCTZ consists of tightly spaced (up to ~ 100 m) thrust splays (Fig. 3a and b), which
282 cut the overturned Maiolica Fm. and the marly beds of the Scaglia Variegata Alpina Fm. (Fig. 3b).
283 The thrust zone is well exposed along a ~ 100 m long road section that exposes the main thrust and a
284 lower basal splay (Figs. 8 and 9). This domain contains asymmetric and faulted folds within the
285 overturned Maiolica Fm. (Fig. 8b) that exhibit pronounced south-verging geometries (Fig. 9b-d), with
286 ENE-WSW-trending fold axes (Fig. 4b) and axial planes dipping NNW at 45°- 50° (Figs. 4d and 9).
287 Folds exhibit thickened hinges associated with local marl migration from the limbs (Fig. 9e) during

progressive folding. The marly domains in the hinge zones represent centimetric interbeds and are foliated (Fig. 9e), with foliation planes converging toward the hinge. Thrust planes bear slickenlines and stepped calcite slickenfibres indicating a top-to-the SSW sense of shear (Fig. 4c). Discrete, N-dipping (δ = 30° - 40°) second order thrust planes are commonly observed in the back limbs of mesoscopic folds, where they mostly localise along thin marly interbeds (Fig. 9b) or along gently dipping (α = 35° - 40°) bed-bed interfaces. Thrust planes accommodate offsets up to a maximum of a few decimeters (Fig. 9c) and cut across the steeply dipping (β = 78 - 85°) to overturned forelimbs (Fig. 9b and d) at high angle. They are associated with laterally continuous layers and lenses of cataclasite, formed by heterometric calcareous and cherty clasts embedded within a fine-grained cataclastic matrix (Figs. 9c and S2). Clasts are angular and derive from both the hanging wall and footwall and exhibit evidence of rigid-body rotation (Figs. 9c and S2). Sub-horizontal calcite veins locally decorate the thrust planes that cut through the highly dipping bedding in the forelimbs at an angle close to 90° (Fig. 9c).

Within the upper and overturned portion of the Maiolica Fm. (~ 250 m from the main thrust, Figs. 3, 8 and 9a), folds remain asymmetric and strongly verging to the SSE, with back- and forelimbs dipping at 25°- 30° (α) and at 60° - 70° (β), respectively and with axial planes dipping toward the NNW at ~ 60° (Figs. 4d and 9f). Marly interbeds are up to 20 cm thick and pervasively foliated in response to flexural slip and layer parallel shearing during progressive folding. On the gently dipping back limbs, these marly beds are deformed by diffuse foliation fabrics indicating a top-to-SE sense of shear (Fig. 9f).

4.1.3 Footwall of the San Donato - Costa Thrust Zone

The footwall of the SCTZ is characterised by an overturned syncline with the more calcareous portion of the Scaglia Variegata Alpina Fm. and the Scaglia Rossa Fm. in the core (Fig. 3 and b). This domain is characterised by m-scale duplex structures defined by N-dipping (~ 35°) and top-to-the SE

floor and roof thrusts (Fig. 10b and c). The stratigraphic succession above and below the duplexes is tabular and undeformed (Fig. 10b and c). Roof thrusts (Fig. 10d and e) dip to the NW (δ = 15°- 35°) and invariably cut across the steeply dipping forelimbs (β = 60°) with a cut-off angle of ~ 45° (Fig. 10e). Within the duplexes, centimetric to decimetric horses and asymmetric lithons made of cherty beds and calcareous portions of Scaglia Rossa Fm. are embedded within pervasively foliated marls (Fig. 10b).

Moving toward the south into the upright limb of the footwall syncline, folds become more verging and asymmetric, defined by S-dipping (β = 75°- 85°) or even overturned (β = 45°- 60°) N-dipping forelimbs, whereas back limbs invariably dip toward the N-NE (α = 25°- 35°; Fig. 10d). Axial planes dip NE at ~50° and fold axes trend ENE-WSW (Fig. 4a and b). Folds are commonly dissected by multiple N-dipping thrust splays that dip (δ) at ~ 20°- 30° and cut the fold hinge or the steeply dipping/overturned forelimbs (Fig. 10d). Interbed thrust planes commonly occur in the back limbs and extend toward the foreland (e.g., toward the south) cutting across the steep overturned forelimbs (β = 67°-79°; Fig. 10d). Weakly foliated cataclastic domains occur where thrusts cut the overturned forelimbs and the siliceous beds, mainly within the footwall of the thrusts (Fig. 10d and e). Deformation is particularly significant in the immediate surroundings of the main thrust surfaces (Fig. 10d and e), as shown by increased fracture densities and locally weakly foliated cataclastic domains (Fig. 10e). On the contrary, foliated domains develop mainly where the thrusts exploit (on the back limbs) or cut (on the forelimbs) weaker marly beds (Figs. 10d and e). Foliation in marly beds is decorated by slickenlines and calcite slickenfibres indicating a top-to-the SSW sense shear (Figs. 4c and 10e). Calcareous sigmoidal lithons are embedded within the foliated marly domains (Fig. 10f). Foliated domains are bounded to the top and bottom by siliceous and stronger beds, which represent the mechanically strongest portion of the succession (Fig. 10d). All the kinematic indicators (slickenlines, calcite slickenfibres, and oblique foliation) are concordant with a top-to-the SSW sense of shear (Fig. 4c).

338 **4.2 X-ray diffraction of representative rock types**

339 **4.2.1 Calcareous beds**

340 The results of the X-ray semiquantitative analyses are shown in Tables S1. Despite differences
341 of stratigraphic age and structural position with respect to the main thrust surface, the mineralogical
342 assemblage of limestone within the SCTZ sedimentary succession is quite similar throughout the
343 entire analysed succession.

344 The limestone samples of the Maiolica Fm. belong to both the hanging wall (samples CZ2042,
345 CZ2043, CZ2044, CZ2045, Fig. 3b) and footwall of the SCTZ (sample CZ2046, Fig. 3b). Their
346 whole-rock composition is characterised by calcite contents between 91 wt % and 98 wt %,
347 subordinate quartz (from 1 wt % to 7 wt %) and traces of Na-plagioclase and phyllosilicate minerals
348 (K-white micas) that never exceed 2 wt %. Occasionally, traces of dolomite and rutile occur (sample
349 CZ2042). Compared to the others, sample CZ2044 contains more quartz (13 wt %) because of the
350 high radiolarian content and lower calcite amounts (85 wt %) than the rest of the samples.

351 The calcareous beds from the Scaglia Variegata Alpina Fm. (samples CZ2047, CZ2048,
352 CZ2049, Fig. 3b) in the footwall domain of the SCTZ are composed of calcite with contents ranging
353 from 93 wt % and 95 wt % and quartz that amounts to 3 - 5 wt %. Na-plagioclase and phyllosilicate
354 minerals (K-white micas) occur with percentages lower than 2 wt %.

355 The Scaglia Rossa Fm. at the core of the footwall domain (Fig. 3b), contain calcite with contents
356 between 82 wt % and 92 wt % and quartz that reaches up to 15 wt %. Accessory phases are albite,
357 phyllosilicates (K-white micas) and hematite (Table S1).

358

359 **4.2.2 Calcareous-marly beds**

360 Calcareous-marly samples exhibit a stronger compositional variability than the limestone
361 (Table S2). Samples from the Maiolica Fm. belong to the hanging wall (CZ2042Ma, CZ2043Ma, Fig.

362 3b) and footwall domains (CZ2052Ma, Fig. 3b). Samples CZ2042Ma, CZ2043Ma, from the upper
363 portion of the Maiolica Fm., are composed of calcite (from 32 wt % to 72 wt %), quartz (15 - 37 wt
364 %), phyllosilicate (9 - 27 wt %) and minor amounts of K-feldspar (< 3 wt %) and albite (> 3 wt %,
365 Table 2). Sample CZ2052Ma, from the medium portion of the Maiolica Fm., displays a mineral
366 assemblage and weight percent similar to those observed in the limestone with a slightly higher
367 content of phyllosilicate (K-white mica, chlorite and mixed layered minerals). The higher quartz
368 amount (37 wt %, sample CZ2042Ma, Table S2) is probably due to a local increase of the radiolarian
369 content within the marly-calcareous matrix of the Maiolica Fm.

370 Calcareous marls from the Scaglia Variegata Alpina Fm. were collected in the footwall of the
371 STCZ. Sample CZ2047Ma close to the thrust surface contains calcite (79 wt %), quartz (11 wt %),
372 phyllosilicate (8 wt %, K-white mica, chlorite and mixed layered minerals), albite (2 wt %) and traces
373 of hematite. Sample CZ2049Ma (Table S2), 500 m far away from the principal thrust surface (Fig.
374 3a and b) has the same mineral content of the limestone samples with calcite weight percent of 95%
375 and minor amounts of phyllosilicate minerals (3 wt %, K-white mica, chlorite and mixed layered
376 minerals) and quartz (2 wt %).

377 Calcareous marls from the Scaglia Rossa Fm. at the core of the footwall syncline of the SCTZ
378 (Fig. 3b) contain calcite as the most abundant mineral (90 - 93 wt %) followed by quartz (3-4 wt %).
379 Furthermore, such samples display higher contents of phyllosilicate minerals (K-white mica and
380 chlorite) than their limestone counterpart that amounts to 3 – 6 wt % of the overall composition.

381

382 **5. Data analysis, interpretation, and parametrisation**

383 We use our field observations and X-ray analyses to constrain the parameters that we believe
384 have played a role in governing deformation and strain localisation within the studied carbonate
385 succession. These are i) the thickness- and ii) the spatial distribution of marly layers, iii) the rock type

and phyllosilicate content and, finally, iv) the geometry of folds and thrusts. Although fluids are known to play a primary role in modulating (or influencing) deformation processes during progressive deformation (e.g., Sibson, 1994; Beaudoin et al., 2014; Curzi et al., 2020, 2021; Marchesini et al., 2019), only a few syn-tectonic mineralisations (calcite slickenfibres and veins) are locally observed in the study area. Hence, our analysis just considers the role played by the primary features (i.e., lithology, bedding) of the involved multilayer succession and does not explicitly account for fluid presence, composition and potential overpressuring.

5.1 Thickness of marly layers

We define a parameter to express the influence of the thickness of marly layers (t1; Fig. 11) in 1 m of stratigraphic section by referring to the following dimensionless ratio:

$$\frac{\sum t_m}{T}\,\%$$

where $\sum t_m$ is the cumulative measured thickness of marly layers in a reference stratigraphic section and *T* is the total measured stratigraphic thickness of the reference section. This ratio is highly variable throughout the studied succession. The Scaglia Rossa Fm. reaches values up to 43 % (Fig. 11a) and even 80 % in its upper portion, while the Maiolica Fm. exhibits the lowest calculated value (3 % - 24 %, Fig. 11b). The parameter is intrinsically scale independent such that it can be applied to all scales of observation. Based on it, we define two representative endmembers to account for the deformation style of the entire studied stratigraphic succession: i) Scaglia Rossa type, with $\sum t_m/T$ = 45 % (Fig. 11a), and ii) Maiolica type, with $\sum t_m/T$ = 10 % (Fig. 11b).

409 **5.2 Spatial distribution of marly layers**

410 The spatial distribution of marly layers within a measured multilayer succession (Fig. 11a and
411 b) can be described by the ratio:

412 $$\frac{N_m}{T}\ (\mathrm{m}^{-1})$$

413 where N_m represents the cumulative number of marly layers within the measured succession, and T
414 describes the reference stratigraphic thickness (1 m). The spatial distribution of marly layers also
415 accounts for the thickness variation between marly (t1) and calcareous (t2) beds (Fig. 11a and b).

416 Within the analysed succession, the spatial distribution of the layers is generally regular, and their
417 thickness seldomly exhibits significant changes. Marly beds are commonly thinner than calcareous
418 beds. The Scaglia Rossa type endmember has $N_m/T = 3 - 5\ m^{-1}$ ratio (Fig. 11a). The Maiolica type
419 endmember, on the other hand, is described by $N_m/T = 1 - 2\ m^{-1}$ (Fig. 11b), with only one or two marly
420 layers within the measured succession. This chosen representative ratio for the endmembers is 3 m^{-1}
421 for the Scaglia Rossa type (Fig. 11a), and 1 m^{-1} for the Maiolica type (Fig. 11b).

422

423 **5.3 Lithology and phyllosilicates content**

424 The XRD data (Tables S1 and S2) of calcareous and calcareous-marly beds reveal that the
425 main differences between the Maiolica and Scaglia Rossa types are exclusively due to the
426 composition of the calcareous beds (Table S1). We consider the Maiolica type as composed of and
427 best represented by calcareous beds where the phyllosilicate content is basically null (sample
428 CZ2045, calcite = 98 wt %, phyllosilicates = 0 wt %; Table S1). The Scaglia Rossa type, instead, is
429 represented by calcareous beds with a significantly lower calcite and higher phyllosilicate content
430 with respect to the Maiolica type (sample CZ2051, calcite = 82 wt %, phyllosilicate = 2 wt %; Table
431 S1).

The composition of the marly beds (Table S2), on the other hand, does not warrant the identification of the two principal endmembers. The composition of the calcareous-marly beds does not show a stark composition change within the succession, and we suggest that the role of marly beds is better accounted for by referring to other parameters ($\sum t_m/T$ and N_m/T, chapters 5.1 and 5.2).

We conclude that while the composition of calcareous-marly beds can be neglected when assessing the role of rock composition on the bulk deformation style, the variable composition of the calcareous beds does play a role. This is accounted for by the two endmembers proposed for our multilayer succession.

5.4 Geometry of folds and thrusts

Our field observations constrain the geometrical relationships between the attitude of minor thrusts and the orientation of folded beds with respect to the imposed stress field during shortening. We consider the variation of the angle between bedding-parallel minor thrusts developed along the fold back limbs (α; Fig. 11c) and the steeply dipping forelimbs (β; Fig. 11d). This angle progressively increases as a fold tightens and amplifies during its continuous evolution, eventually leading to fold asymmetry and vergence. We note that in our field case study:

- α is quite constant throughout the structural domains, and rarely exceeds 40° (Fig. 4a), with an average of ~ 36° (Fig. 11c).
- β exhibits a greater variability (Fig. 11d), varying between 34° and 90° (for the upright folds), with an average of ~ 65°, due to the progressive steepening of forelimbs. In the overturned folds, β ranges between 50° and 85°, defining an average value of ~ 73° (Fig. 11d).
- δ is comparable in the hanging wall, thrust zone and footwall domains (Fig. 11e), rarely exceeding 45° and with an average value of 36°.

In summary, δ and α share similar values between 30° and 35° throughout the hanging wall, thrust zone and footwall domains (Fig. 11c and e). δ and β are, instead, very different from each other, with a dip angle average of 35° for δ and 60°- 73° for β (Fig. 11d and e).

6. Discussion

6.1 A conceptual deformation model

By integrating field observations and the semiquantitative approach illustrated above, we now propose a conceptual deformation model for the structural evolution of a carbonate multilayer succession from its undeformed stage (Figs. 12a and 13a), through an intermediate folding phase (Figs. 12b-c and 13b-c) to a final faulting stage (Figs. 12d and 13d). We discuss the evolution of the studied structures through time to highlight the progressive activation/deactivation of the studied deformation processes. We apply the conceptual evolutionary model to the Scaglia Rossa and Maiolica endmembers. Their differences notwithstanding, both deformation models take on from similar evolutions during the first increments of deformation and are described in the following conceptual steps of the progressive deformation:

- *Layer parallel shortening, layer buckling and layer parallel shearing (LPS)*

  Deformation begins with layer parallel shortening eventually causing buckling of the succession (e.g., Whitaker and Bartholomew, 1999; Marques, 2008; Tavarnelli et al., 2021). This induces pervasive pressure solution along solution planes at high angle to bedding (Figs. 5, 12b and 13b). Layer parallel shearing (LPS), on the other hand, governs the first increments of slip along bed-bed interfaces and causes bedding planes to act as early thrust surfaces (Figs. 9, 12b and 13b; e.g., Ez, 2000; Hudleston and Treagus, 2010) as they become optimally oriented during compression. LPS, therefore, marks the transition into non-coaxial deformation from buckling.

- *Folding*

481 The second stage of deformation is represented by the more advanced folding of the
482 multilayer succession (Figs. 12c and 13c). We consider this folding stage as encompassing
483 all those processes that lead to the progressive increase of fold asymmetry as folds
484 progressively evolve from the early symmetric buckle geometry during continued
485 shortening.
486 The increase of the fold asymmetry within the folded multilayer implies a transition from
487 pure shear to simple shear under the same stress field boundary conditions. This transition
488 is commonly associated with rheological contrasts between the layers (Skjernaa, 1979)
489 and/or with the original misorientation between the bedding (the studied succession) and
490 the main fault zone (BT-SCTZ), that cuts across the multilayer (Sanderson, 1979, Casey
491 and Huggenberger, 1985; Rowan and Kligfield, 1992), and with flexural slip processes
492 (Ramsay, 1974; Hudleston and Treagus, 2010). Our observations indicate that early buckle
493 folds (Figs. 5c, 12c and 13c) pass to asymmetric (Fig. 9f) and tight (Fig. 6d) geometries
494 through the steepening of the forelimbs (Figs. 12c and 13c). This increase of asymmetry
495 is accompanied by flexural slip for both the Scaglia Rossa and Maiolica type scenarios.
496 Flexural slip within the Maiolica type ($N_m/T = 1\ m^{-1}$; Fig. 13c) localises principally along
497 the marly beds, whereas within the Scaglia Rossa type ($N_m/T = 3\ m^{-1}$; Fig. 12c) is
498 volumetrically distributed.
499 The two models start to behave differently only during the final phases of this stage of
500 deformation (Figs. 12c and 13c). The Scaglia Rossa type accommodates the progressive
501 steepening and overturning of the forelimbs (Fig. 12c), whereas the Maiolica type
502 develops vertical and only rarely overturned fold forelimbs (Fig. 13c). Moreover, fold
503 hinges of the Maiolica type model undergo progressive volume increase due to the flow
504 of marls from the limbs during the initial stages of folding (Ramsay, 1967, 1974).
505
506 • *Faulting and cataclasis*

This stage of deformation (Figs. 12d and 13d) is accommodated by thrusting, which occurs after folds become locked-up due to their inability to accommodate further shortening by folding (e.g., Tavarnelli, 1997; Ramsay, 1974; Fischer et al., 1992). New thrusts form and localise along bed-bed interfaces on the fold back limbs (where $\delta \sim \alpha$) and are driven by layer parallel shortening (Figs. 12d and 13d). Thrust surfaces cut across the verticalised or overturned forelimbs (where $\beta >> \delta$), while LPS occurs on suitably oriented back limbs (Figs. 12d and 13d) until after the folding-faulting transition. The observed thrusts are compatible with what has been previously described as "*long limb thrust*" or "*long limb detachment*" (e.g., Alonso and Teixell, 1992; Marques et al., 2010), which are indeed discrete slip surfaces that are sub-parallel to gently dipping limb and cut steeply-dipping or verticalised limb within asymmetric folds. For both the Maiolica and Scaglia Rossa types, faults slip first on the back limb, because of continuous folding-related flexural slip (Figs. 12d and 13d), and subsequently cut the steeply dipping limb.

The two endmember models strongly differ significantly in the faulting stage. Deformation is strongly distributed within the Scaglia Rossa type and only localises within the calcareous portions of the succession, where cataclasites locally develop. A foliation may form within the marly portions, cutting and transposing the verticalised or overturned fold forelimbs (Figs. 10d-e and 12d). According to Tavarnelli (1997, 2021), the thrust cutting across the forelimb progressively widens after initial localisation due to the progressive coalescence of multiple subsidiary fault planes. While these subsidiary faults develop (Fig. 12d), the thicker marly beds tend to become foliated and to wrap around calcareous lithons (Figs. 10d and f, 12d).

The Maiolica type model, instead, behaves differently due to the preponderance of limestone ($\sum t_m/T$ = 10 %, N_m/T = 1 m^{-1}; Fig. 13d). Limestones deform by fracturing and localised cataclastic flow that are genetically associated with foreland-directed thrust propagation. The increase of deformation along thrusts is accompanied by the evolution

of cataclastic textures, which pass from proto- to ultra cataclasites (e.g., Billi, 2010; Ferraro et al., 2018) decorating the thrust planes between the calcareous beds (Figs. 9b-c and 13d). Cataclasites may locally develop a weak foliation, particularly where the marly domains are affected (Fig. 13d). However, cataclasis is exclusively localised on the forelimbs (Figs. 12d and 13d), where thrusts cut the verticalized limbs at a high cut-off angle.

In both endmember cases, after the beginning of faulting, deformation on the back limbs continues to be accommodated by LPS (Figs. 12d and 13d) with thrusts and reverse faults continuing to localise along bed-bed interfaces.

6.2 Constraining the activation of folding-faulting transition

We have calculated the critical dip angle of fold forelimbs beyond which faulting takes over from folding. Our analysis relies on the study and quantification of 84 folds for which we have systematically measured α and β (Figs. 11c and d, 14a). We propose a new type of plot, which shows the variation of β vs. the β/α ratio (Fig. 14a), which expresses the overall fold asymmetry. 52 readings of unfaulted folds plot in a discrete cluster, with $\beta < 80°$ and $\beta/\alpha < 1.8$ (82 % of the unfaulted folds) and form the low asymmetry fold cluster (upper two green folds in Fig. 14b). The remaining 9 readings (18 %) of the unfaulted folds are characterised by β/α values up to 3.3 (Fig. 14a), marking the transition to significant fold asymmetry (lowermost green fold in Fig. 14b).

The second cluster is represented by the faulted folds (Fig. 11d) with upright limbs, with $\beta \geq 80°$ and $\beta/\alpha \geq 3.3$ (Fig.14a), testifying to a progressive verticalisation of the forelimbs and a related increase of the fold asymmetry (light blue folds in Fig. 14b). One less well-defined cluster is formed by the overturned faulted folds (Fig. 14a). Due to the progressive overturning of the forelimbs (orange folds in Fig. 14b), both β and β/α values tend to decrease. β shows here a greater dispersion (50 - 85°)

557 with respect to the upright folds (Fig. 14a and b), whereas the β/α ratio is generally ≥ 1.8, partially
558 overlapping the folding domain (Fig. 14a).

559 We also consider the normal distribution and frequency of β for 28 faulted folds (Fig. 14c).
560 Considering the upright faulted folds (light blue), ~ 80 % of the readings of β lie within the 83°- 90°
561 interval (Fig. 14c), whereas β of the overturned folds shows a more dispersed pattern (Fig. 14c),
562 ranging from 50° to 87°. The normal distribution of β for the upright faulted folds shows an average
563 of ~ 83° (Fig. 14c), consistent with Fig. 14a, while an average of ~ 73° (Fig. 14c) represents the
564 normal distribution of β for the overturned folds.

565 To sum up, our quantification demonstrates that α and β are appropriate geometrical parameters
566 to describe the conditions whereby the transition from folding to faulting occurs during progressive
567 shortening. In particular, β close to 80° and β/α ≥ 3.3 are critical threshold values to enable the
568 beginning of thrusting from mature folding (Figs. 12, 13 and 14). Once the threshold is reached,
569 thrusts form, propagate, and cut across the verticalised or overturned forelimbs (Fig. 14b). Thus, our
570 model postulates that fold asymmetry (as neatly expressed by the β/α ratio) is key in steering
571 deformation, in agreement with insights from numerical modelling, where faulting is favoured as fold
572 asymmetry increases (e.g., Simpson, 2009; Humair et al., 2020).

573

574 **6.3 Implications on deformation style and seismic behaviour**

575 When combined with considerations on the rock types forming the deformed multilayer, the
576 definition of a critical limb dip angle to faulting (~ 80°) has strong implications upon the
577 understanding of the deformation style and seismic behaviour in fold-and-thrust belts, which we
578 discuss here by referring to the conceptual scheme of Figure 15. Our results show that during folding
579 (when β < 80° and β/α < 3.3) carbonate multilayers may deform aseismically (Fig. 15a), with
580 deformation being mostly accommodated by flexural slip along weak (marly) bed-bed interfaces (Fig.

581 15a). Upon reaching the critical β = 80° and β/α = 3.3 values (time t_1, Fig. 15b), however, forelimbs
582 lock up and begin to store stress according to a "stick" mechanical behaviour (Brace and Byerlee,
583 1966; Fig. 15b). Layer parallel shearing remains active in the back limbs (Fig. 15b), which
584 accommodate strain aseismically by exploiting the weak marly beds of the deforming multilayer (Fig.
585 15b). Coseismic rupturing ("slip" behaviour, Brace and Byerlee, 1966; time t_2 in Fig. 15b) eventually
586 localises when the rock strength in the forelimbs is finally overcome and a discrete Principal Slip
587 Surface forms (PSS; Fig. 15b). At this stage, folds are "deactivated", decapitated by thrusts, and
588 further deformation is taken up exclusively by discrete localised faulting. The overall rheology of the
589 system becomes thus governed by the mechanics of the newly formed fault, whereas, on the back
590 limbs, strain is continuously accommodated by aseismic layer parallel shearing (Fig. 15c). Cyclically,
591 continuous shortening will lead to critical conditions for renewed seismic rupturing (time t_3, t_4, t_n)
592 along the thrust surfaces. For each coseismic rupture, thrusts may widen, for example by the
593 formation and coalescence of cataclasites (Fig. 15c).

594 In summary, during and after the folding-faulting transition (Figs. 12d, 13d, 15), the system we
595 describe can simultaneously host two different styles of deformation: i) discrete brittle deformation
596 along discrete thrusts accompanied by seismic rupturing on the forelimbs (Fig. 15c), which, upon
597 continuous shortening, end up being highly misoriented to the imposed stress field (Figs. 9b-d and
598 10d-e), and ii) aseismic creep on suitably oriented back limbs, (Figs. 12d, 13d, 15), which forms
599 variably-sized foliated domains within the marly parts of the deforming multilayer succession (Fig.
600 10f).

601

602 **6.4 Upscaling of the deformation model**

603 Our conceptual deformation model and its implications on seismic behaviour are of great
604 potential interest when considering the seismotectonic framework and the seismic hazard of active
605 fold-and-thrust belts deforming carbonate multilayer successions, like the ESA. The up-scaled

606 applicability of the results derived in this study obviously needs to be thoroughly investigated and
607 validated against real case scenarios where geophysical data are of sufficient quality to allow exact
608 spatial correlations between earthquake hypocentres and the geometry of folds and thrusts. To that
609 end, however, we first need to assess whether our results are (meso)scale-dependent or can instead
610 be extrapolated to the much larger dimensions of entire belts. Our model relies on numerical ratios
611 (i.e., $\sum t_m/T$, N_m/T) and values (i.e., α, β, δ and β/α ratio) that are used to characterise rock type and
612 structural geometry, respectively. These are dimensionless parameters, such that they can also be used
613 to describe thicker (km-thick) multilayer successions or to characterise the geometrical relationships
614 between back- and forelimbs aiming to constrain the evolution of km-scale folds.

615 The possibility to upscale our findings is also justified by the cyclic nature of sedimentation
616 within carbonate multilayer successions. This cyclicity, which principally reflects recurrent and
617 periodic environmental changes during sedimentation, is documented by the interbedding of
618 terrigenous- (e.g., marl) and calcareous- beds/units, ad is present at all scales of observation due to
619 different temporal amplitudes of the sedimentation cycles (i.e., from hundreds of My to hundreds of
620 ky). In this scenario, the interlayering of pure calcareous and marly formations (e.g., reflecting
621 temporal cycles on the hundreds of My scale) represents the effects of high-amplitude sedimentation
622 cycles, whereas the interlayering of mesoscale beds represents the effects of low- amplitude cycles
623 (e.g., hundreds of ky). As described above, multilayer carbonate successions share similar
624 stratigraphic and architectural features at different scales of observation, confirming that our
625 parametric approach can be readily applied to also thicker successions.

626 Lastly, our results are applicable in different geological contexts if we consider our system as an
627 analogue of a "standard" carbonate pelagic succession, composed of several sedimentary cycles. All
628 local heterogeneities notwithstanding, the described succession can be considered as an appropriate
629 mechanical analogue of carbonate multilayer successions elsewhere, irrespective of stratigraphic age
630 (Neoproterozoic, Oman Mountains, Allen, 2007; Mesozoic, Lesser Caucasus, Gusmeo et al., 2021;

631 Palaeozoic – Cenozoic, Western Alps, Decarlis et al., 2013; Meso – Cenozoic, Central Apennines,
632 Fabbi, 2014; Cipriani, 2019). For instance, the specific sedimentological and architectural features of
633 the analysed succession (Fig. 3c) are representative of many successions associated with rifting
634 related to the opening of the Tethyan Ocean, now exposed in several peri-Mediterranean areas and in
635 fold-and-thrust belts moving from Cuba to Japan (e.g., Wieczorek, 1988; Masse et al., 1995; Bernoulli
636 and Jenkyns, 2009).

637

638 **7. Conclusions**

639 The carbonate multilayer succession affected by the San Donato-Costa Thrust Zone (Eastern
640 Southern Alps of Italy) has allowed us to explore and constrain the parameters that govern the folding-
641 faulting transition during shortening in carbonate multilayer successions. Our data confirm that the
642 mechanical stratigraphy of the deforming multilayer plays a key role in governing the bulk style of
643 deformation and deformation partitioning in the carbonate and marly endmembers of compositionally
644 heterogeneous multilayers. Deformation progresses from i) layer parallel shortening, layer parallel
645 shearing and incipient buckling, through ii) buckling and folding, to iii) faulting and cataclasis. Our
646 conceptual evolutionary model suggests that this evolution is accommodated by fold amplification
647 and increasing asymmetry until post-folding faulting activates. For the first time, we quantitatively
648 determined a critical angle threshold for the transition from folding to faulting, which we link to the
649 progressive increase of the dip angle of back limbs (α) and forelimbs (β). This threshold, which
650 corresponds to $\beta \geq 80°$ and $\beta/\alpha \geq 3.3$, represents the condition for faulting to take over from folding
651 in a multilayer carbonate-dominated succession.

652 This purely geometrical set of constraints is intrinsically scale-independent and can, therefore,
653 be applied to the scale of an entire fold-and-thrust-belt aiming at exploring, for example, the
654 geometrical-structural conditions that control hypocentre location within a seismically deforming
655 carbonate multilayer succession. Insights from this study help to improve our understanding of

distributed deformation localisation and seismic rupturing and may prove useful to better assess the seismotectonic framework and seismic hazard of active fold-and-thrust belts affecting multilayer carbonate successions.

Acknowledgments

The authors thank Francesca Stendardi for her support in the field. Angelo Cipriani is thanked for the fruitful discussion about the stratigraphy of the area. Alberto Ceccato is thanked for his support and the discussion concerning the data analysis. The present work benefited from the fruitful and constructive reviews of two anonymous reviewers. We thank Fabrizio Agosta for the editorial handling and for useful comments on the final version of the manuscript.

Funding

This work belongs to the PhD project "Structural characterisation of selected thrust zones in the Eastern Southern Alps and Northern Oman: implication on strain localisation and seismogenesis in carbonates" of the first author.

Reference

Allen, P. A., 2007. The Huqf Supergroup of Oman: basin development and context for Neoproterozoic glaciation. Earth-Science Reviews 84(3-4), 139-185. http://dx.doi.org/10.1016/j.earscirev.2007.06.005.

Alonso, J., L. & Teixell, A., 1992. Forelimb deformation in some natural examples of fault-propagation folds. In: Thrust tectonics. Springer, Dordrecht, 1992. 175-180. https://doi.org/10.1007/978-94-011-3066-0_15.

Anderlini, L., Serpelloni, E., Tolomei, C., Marco De Martini, P., Pezzo, G., Gualandi, A., and Spada, G., 2020. New insights into active tectonics and seismogenic potential of the Italian Southern Alps from vertical geodetic velocities. Solid Earth 11, 1681–1698. https://doi.org/10.5194/se-11-1681-2020.

680 Anselmi, M., Govoni, A., De Gori, P., and Chiarabba, C., 2011. Seismicity and velocity structures along the
681 south-Alpine thrust front of the Venetian Alps (NE-Italy). Tectonophysics 513, 37–48.
682 https://doi.org/10.1016/j.tecto.2011.09.023.

683 Beaudoin, N., Bellahsen, N., Lacombe, O., Emmanuel, L., and Pironon, J., 2014. Crustal- scale fluid flow
684 during the tectonic evolution of the Bighorn Basin (Wyoming, USA). Basin Research 26(3), 403-435.
685 http://dx.doi.org/10.1111/bre.12032.

686 Bernoulli, D., and Jenkyns, H. C., 2009 . Ancient oceans and continental margins of the Alpine-Mediterranean
687 Tethys: Deciphering clues from Mesozoic pelagic sediments and ophiolites. Sedimentology 56(1), 149–
688 190. https://doi.org/10.1111/j.1365-3091.2008.01017.x.

689 Bigi, S., Pisani, P. C., Tavarnelli, E., Calamita, F., & Paltrinieri, W., 2003. The" pre-thrusting" Fiamignano
690 normal fault. Bollettino della Società geologica italiana 122(2), 267-276.

691 Billi, A., Salvini, F., and Storti, F., 2003. The damage zone-fault core transition in carbonate rocks:
692 implications for fault growth, structure and permeability. Journal of Structural geology 25(11), 1779-
693 1794. https://doi.org/10.1016/S0191-8141(03)00037-3.

694 Billi, A., 2010. Microtectonics of low-P low-T carbonate fault rocks. Journal of Structural Geology 32(9),
695 1392-1402. https://doi.org/10.1016/j.jsg.2009.05.007.

696 Bosellini, A., Masetti, D., and Sarti, M., 1981. A Jurassic 'tongue of the ocean' infilled with oolitic sands: The
697 Belluno Trough, Venetian Alps, Italy. Marine Geology 44(1–2),
698 59–95. https://doi.org/10.1016/0025-3227(81)90113-4.

699 Bosellini, A., Gianolla, P., & Stefani, M., 2003. Geology of the Dolomites. Episodes 26(3), 181-185.
700 https://doi.org/10.18814/epiiugs/2003/v26i3/005.

701 Brace, W. F., and Byerlee, J. D., 1966. Stick-slip as a mechanism for earthquakes. Science 153(3739), 990-
702 992. https://doi.org/10.1126/science.153.3739.990.

703 Bullock, R.J., De Paola, N., Holdsworth, R.E., and Trabucho-Alexandre, J., 2014. Lithological controls on the
704 deformation mechanisms operating within carbonate-hosted faults during the seismic cycle: Journal of
705 Structural Geology 58, 22–42. https://doi.org/10.1016/j.jsg.2013.10.008.

706 Butler, R. W., Maniscalco, R., and Pinter, P. R., 2019. Syn-kinematic sedimentary systems as constraints on
707 the structural response of thrust belts: re-examining the structural style of the Maghrebian thrust belt of
708 Eastern Sicily. Italian Journal of Geosciences 138(3), 371-389. https://doi.org/10.3301/IJG.2019.11.

709 Butler, R.W.H., Bond, C.E., Cooper, M.A., and Watkins, H., 2020, Fold–thrust structures – Where have all
710 the buckles gone? Geological Society Special Publication 487, 21–44. https://doi.org/10.1144/SP487.7.

711 Caputo, R., Poli, M.E., Zanferrari, A., 2010. Neogene-Quaternary tectonic stratigraphy of the eastern Southern
712 Alps, NE Italy. Journal of Structural Geology 32, 1009-1027.
713 http://dx.doi.org/10.1016/j.jsg.2010.06.004.

714 Carminati, E., Doglioni, C., and Scrocca, D., 2004. Alps Vs Apennines: Special Volume of the Italian
715 Geological Society, 141–151.

716 Carminati, E., Enzi, S., and Camuffo, D., 2007. A study on the effects of seismicity on subsidence in foreland
717 basins: An application to the Venice area: Global and Planetary Change 55, 237–250.
718 https://doi.org/10.1016/j.gloplacha.2006.03.003.

719 Carminati, E., Aldega, L., Trippetta, F., and Kavoosi, M.A., 2018. Zagros fold and thrust belt in the Fars
720 province (Iran) I: Control of thickness/rheology of sediments and pre-thrusting tectonics on structural
721 style and shortening. Marine and Petroleum Geology 91, 211-224.
722 https://doi.org/10.1016/j.marpetgeo.2018.01.005.

723 Casey, M., & Huggenberger, P., 1985. Numerical modelling of finite-amplitude similar folds developing under
724 general deformation histories. Journal of Structural Geology 7(1), 103-114.
725 https://doi.org/10.1016/0191-8141(85)90118-X.

726 Castellarin, A., Lucchini, F., Rossi, P. L., Selli, L., and Simboli, G., 1988. The Middle Triassic magmatic-
727 tectonic arc development in the Southern Alps. Tectonophysics 146(1-4), 79-89.
728 https://doi.org/10.1016/0040-1951(88)90083-2.

729 Castellarin, A., and Cantelli, L., 2000. Neo-Alpine evolution of the Southern Eastern Alps. Journal of
730 Geodynamics 30, 251–274. https://doi.org/10.1016/S0264-3707(99)00036-8.

731 Castellarin, A., Nicolich, R., Fantoni, R., Cantelli, L., Sella, M., and Selli, L., 2006. Structure of the lithosphere

732 beneath the Eastern Alps (southern sector of the TRANSALP transect). Tectonophysics 414, 259–282.
733 https://doi.org/doi:10.1016/j.tecto.2005.10.013.

734 Cheloni, D., D'Agostino, N., & Selvaggi, G., 2014. Interseismic coupling, seismic potential, and earthquake
735 recurrence on the southern front of the Eastern Alps (NE Italy). Journal of Geophysical Research: Solid
736 Earth 119(5), 4448-4468. https://doi.org/10.1002/2014JB010954.

737 Chiarabba, C., Jovane, L., and DiStefano, R., 2005. A new view of Italian seismicity using 20 years of
738 instrumental recordings. Tectonophysics 395(3-4), 251-268.
739 http://dx.doi.org/10.1016/j.tecto.2004.09.013.

740 Cilona, A., Baud, P., Tondi, E., Agosta, F., Vinciguerra, S., Rustichelli, A., and Spiers, C. J., 2012.
741 Deformation bands in porous carbonate grainstones: Field and laboratory observations. Journal of
742 Structural Geology 45, 137-157. https://doi.org/10.1016/j.jsg.2012.04.012.

743 Cilona, A., Faulkner, D. R., Tondi, E., Agosta, F., Mancini, L., Rustichelli, A., ... & Vinciguerra, S., 2014. The
744 effects of rock heterogeneity on compaction localization in porous carbonates. Journal of Structural
745 Geology 67, 75-93. https://doi.org/10.1016/j.jsg.2014.07.008.

746 Cipriani, A., 2019. Geological map of the central part of Narni-Amelia Ridge (Central Apennines,
747 Italy). Geological Field Trips & Maps 11(2.2). http://dx.doi.org/10.3301/GFT.2019.04.

748 Collettini, C., Niemeijer, A., Viti, C., and Marone, C., 2009. Fault zone fabric and fault
749 weakness. Nature 462(7275), 907-910. https://doi.org/10.1038/nature08585.

750 Collettini, C., Viti, C., Tesei, T., and Mollo, S., 2013. Thermal decomposition along natural carbonate faults
751 during earthquakes. Geology 41, 927–930. https://doi.org/10.1130/G34421.1.

752 Curzi, M., Aldega, L., Bernasconi, S.M., Berra, F., Billi, A., Boschi, C., Franchini, S., Van der Lelij, R., Viola,
753 G., and Carminati, E., 2020. Architecture and evolution of an extensionally-inverted thrust (Mt. Tancia
754 Thrust, Central Apennines): Geological, structural, geochemical, and K–Ar geochronological
755 constraints. Journal of Structural Geology 136, 104059, https://doi.org/doi:10.1016/j.jsg.2020.104059.

756 Curzi, M., Bernasconi, S. M., Billi, A., Boschi, C., Aldega, L., Franchini, S., Albert, R., Gerdes, A., Barberio,

M. D., Looser, N., & Carminati, E., 2021. U-Pb age of the 2016 Amatrice earthquake causative fault (Mt. Gorzano, Italy) and paleo-fluid circulation during seismic cycles inferred from inter-and co-seismic calcite. Tectonophysics 819, 229076. http://dx.doi.org/10.1016/j.tecto.2021.229076.

Dautriat, J., Bornert, M., Gland, N., Dimanov, A., & Raphanel, J. 2011. Localized deformation induced by heterogeneities in porous carbonate analysed by multi-scale digital image correlation. Tectonophysics 503(1-2), 100-116. https://doi.org/10.1016/j.tecto.2010.09.025.

D'Alberto, L., Boz, A., and Doglioni, C., 1995. Structure of the Vette Feltrine (Eastern Southern Alps). Memorie Della Società Geologica Italiana 47, 189–199.

D'Ambrogi, C., and Doglioni, C., 2008. Struttura delle Vette Feltrine. Rendiconti Online Societa Geologica Italiana 4, 37–40.

De Min, A., Velicogna, M., Ziberna, L., Chiaradia, M., Alberti, A., & Marzoli, A., 2020. Triassic magmatism in the European Southern Alps as an early phase of Pangea break-up. Geological Magazine 157(11), 1800-1822. https://doi.org/10.1017/S0016756820000084.

Decarlis, A., Dallagiovanna, G., Lualdi, A., Maino, M., & Seno, S., 2013. Stratigraphic evolution in the Ligurian Alps between Variscan heritages and the Alpine Tethys opening: A review. Earth-Science Reviews 125, 43-68. https://doi.org/10.1016/j.earscirev.2013.07.001.

Delle Piane, C., Clennell, M. B., Keller, J. V., Giwelli, A., and Luzin, V., 2017. Carbonate hosted fault rocks: A review of structural and microstructural characteristic with implications for seismicity in the upper crust. Journal of Structural Geology 103, 17-36. https://doi.org/10.1016/j.jsg.2017.09.003.

Doglioni, C., 1987. Tectonic of the Dolomites (Southern Alps, Northern Italy). Journal of Structural Geology 9, 181–193. https://doi.org/10.1016/0191-8141(87)90024-1.

Doglioni, C., 1990. Thrust tectonic examples from the Venetian Alps. Studi Geologici Camerti, 117-129.

Doglioni, C., 1992. The Venetian Alps thrust belt. In Thrust tectonics (319-324). Springer, Dordrecht.

Doglioni, C., and Carminati, E., 2008. Structural styles and Dolomites field trip. Memorie Descrittive della Carta Geologica d'Italia 82, 1–299.

782 Erickson, S.G., 1996. Influence of mechanical stratigraphy on folding vs faulting. Journal of Structural
783 Geology 18, 443–450. https://doi.org/10.1016/0191-8141(95)00064-K.

784 Ez, V., 2000. When shearing is a cause of folding. Earth-Science Reviews 51(1-4), 155-172.
785 https://doi.org/10.1016/S0012-8252(00)00020-9.

786 Fabbi, S., 2014. Geology and Jurassic paleogeography of the Mt. Primo-Mt. Castel Santa Maria ridge and
787 neighbouring areas (Northern Apennines, Italy). Journal of Maps 11(4), 645-663.
788 https://doi.org/10.1080/17445647.2014.956235.

789 Fagereng, Å., Hillary, G. W., and Diener, J. F., 2014. Brittle- viscous deformation, slow slip, and
790 tremor. Geophysical Research Letters 41(12), 4159-4167. http://dx.doi.org/10.1002/2014GL060433.

791 Ferraro, F., Grieco, D. S., Agosta, F., & Prosser, G., 2018. Space-time evolution of cataclasis in carbonate fault
792 zones. Journal of Structural Geology 110, 45-64. https://doi.org/10.1016/j.jsg.2018.02.007.

793 Fischer, M.P., Woodward, N.B., and Mitchell, M.M., 1992. The kinematics of break-thrust folds. Journal of
794 Structural Geology 14, 451–460. https://doi.org/10.1016/0191-8141(92)90105-6.

795 Fischer, M.P., and Jackson, P.B., 1999. Stratigraphic controls on deformation patterns in fault-related folds: A
796 detachment fold example from the Sierra Madre Oriental, northeast Mexico. Journal of Structural
797 Geology 21, 613–633. https://doi.org/10.1016/S0191-8141(99)00044-9.

798 Fossen, H., 2016. Structural geology. Cambridge university press.

799 Galadini, F., Poli, M.E., and Zanferrari, A., 2005. Seismogenic sources potentially responsible for earthquakes
800 with M ≥ 6 in the Eastern Southern Alps (Thiene-Udine sector, NE Italy). Geophysical Journal
801 International 161, 739–762. https://doi.org/10.1111/j.1365-246X.2005.02571.x.

802 Giorgetti, C., Collettini, C., Scuderi, M.M., Barchi, M.R., and Tesei, T., 2016. Fault geometry and mechanics
803 of marly carbonate multilayers: An integrated field and laboratory study from the Northern Apennines,
804 Italy. Journal of Structural Geology 93, 1–16, https://doi.org/10.1016/j.jsg.2016.10.001.

805 Gusmeo, T., Cavazza, W., Alania, V. M., Enukidze, O. V., Zattin, M., & Corrado, S., 2021. Structural inversion
806 of back-arc basins–The Neogene Adjara-Trialeti fold-and-thrust belt (SW Georgia) as a far-field effect

807 of the Arabia-Eurasia collision. Tectonophysics 803, 228702.
808 https://doi.org/10.1016/j.tecto.2020.228702.

809 Handy, M. R., Schmid, S. M., Bousquet, R., Kissling, E., and Bernoulli, D., 2010. Reconciling plate-tectonic
810 reconstructions of Alpine Tethys with the geological–geophysical record of spreading and subduction
811 in the Alps. Earth-Science Reviews 102(3-4), 121-158. https://doi.org/10.1016/j.earscirev.2010.06.002.

812 Hudleston, P.J., Treagus, S.H., and Lan, L., 1996. Flexural flow folding: Does it occur in nature? Geology 24,
813 203–206. https://doi.org/10.1130/0091-7613(1996)024%3C0203:FFFDIO%3E2.3.CO;2.

814 Hudleston, P.J., and Treagus, S.H., 2010. Information from folds: A review. Journal of Structural Geology 32,
815 2042–2071, https://doi.org/10.1016/j.jsg.2010.08.011.

816 Humair, F., Bauville, A., Epard, J.L., and Schmalholz, S.M., 2020. Interaction of folding and thrusting during
817 fold-and-thrust-belt evolution: Insights from numerical simulations and application to the Swiss Jura
818 and the Canadian Foothills. Tectonophysics 789, 228474, https://doi.org/10.1016/j.tecto.2020.228474.

819 Ikari, M. J., Niemeijer, A. R., & Marone, C., 2015. Experimental investigation of incipient shear failure in
820 foliated rock. Journal of Structural Geology 77, 82-91. https://doi.org/10.1016/j.jsg.2015.05.012.

821 ISIDe Working Group, 2007. Italian Seismological Instrumental and Parametric Database (ISIDe). Istituto
822 Nazionale di Geofisica e Vulcanologia (INGV). http://doi.org/10.13127/ISIDE.

823 Kamb, W. B., 1959. Ice petrofabric observations from Blue Glacier, Washington, in relation to theory and
824 experiment. Journal of Geophysical Research 64(11), 1891-1909.
825 https://doi.org/10.1029/JZ064i011p01891.

826 Kilian, R., Heilbronner, R., and Stünitz, H., 2011. Quartz grain size reduction in a granitoid rock and the
827 transition from dislocation to diffusion creep. Journal of Structural Geology 33, 1265–1284.
828 https://doi.org/10.1016/j.jsg.2011.05.004.

829 Kilian, S., Ortner, H., and Schneider-Muntau, B., 2021. Buckle folding in the Northern Calcareous Alps-Field
830 observations and numeric experiments. Journal of Structural Geology 150, 104416.
831 https://doi.org/10.1016/j.jsg.2021.104416.

Labaume, P., Carrio-Schaffhauser, E., Gamond, J. F., and Renard, F., 2004. Deformation mechanisms and fluid-driven mass transfers in the recent fault zones of the Corinth Rift (Greece). Comptes Rendus Geoscience 336(4-5), 375-383. https://doi.org/10.1016/j.crte.2003.11.010.

Lacombe, O., Lavé, J., Roure, F. M., & Verges, J. (Eds.), 2007a. Thrust belts and foreland basins: From fold kinematics to hydrocarbon systems. Springer Science & Business Media.

Lena, G., Barchi, M.R., Alvarez, W., Felici, F., and Minelli, G., 2015. Mesostructural analysis of S-Cfabrics in a shallow shear zone of the Umbria-Marche Apennines (Central Italy). Geological Society Special Publication 409, 149–166. https://doi.org/10.1144/SP409.10.

Lustrino, M., Abbas, H., Agostini, S., Caggiati, M., Carminati, E., and Gianolla, P., 2019. Origin of Triassic magmatism of the Southern Alps (Italy): Constraints from geochemistry and Sr-Nd-Pb isotopic ratios. Gondwana Research 75, 218-238. http://dx.doi.org/10.1016/j.gr.2019.04.011.

Marchesini, B., Garofalo, P. S., Menegon, L., Mattila, J., & Viola, G., 2019. Fluid-mediated, brittle–ductile deformation at seismogenic depth–Part 1: Fluid record and deformation history of fault veins in a nuclear waste repository (Olkiluoto Island, Finland). Solid Earth 10(3), 809-838. https://doi.org/10.5194/se-10-809-2019.

Marques, F.O., 2008. Thrust initiation and propagation during shortening of a 2-layer model lithosphere. Journal of Structural Geology 30, 29–38. https://doi.org/10.1016/j.jsg.2007.09.005.

Marques, F. O., Burg, J.-P., Lechmann, S. M. & Schmalholz, S. M., 2010. Fluid assisted particulate flow of turbidites at very low temperature: A key to tight folding in a submarine Variscan foreland basin of SW Europe. Tectonics 29(2). https://doi.org/10.1029/2008TC002439.

Masetti, D., Claps, M., Giacometti, A., Lodi, P., and Pignatti, P., 1998. I Calcari Grigi della Piattaforma di Trento (Lias inferiore e medio, Prealpi Venete). Atti Ticinensi Scienze della Terra 40, 139–183. http://hdl.handle.net/11368/1697434.

Masse, J. P., Philip, J., and Camoin, G., 1995. The Cretaceous Tethys. In The Tethys Ocean 215-236. Springer, Boston, MA.inger, Boston, MA.

Micarelli, L., Benedicto, A., & Wibberley, C. A. J. 2006. Structural evolution and permeability of normal fault zones in highly porous carbonate rocks. Journal of Structural Geology 28(7), 1214-1227. https://doi.org/10.1016/j.jsg.2006.03.036.

Michie, E. A. H., Haines, T. J., Healy, D., Neilson, J. E., Timms, N. E., and Wibberley, C. A. J., 2014. Influence of carbonate facies on fault zone architecture. Journal of Structural Geology 65, 82-99. https://doi.org/10.1016/j.jsg.2014.04.007.

Michie, E.A.H., 2015. Influence of host lithofacies on fault rock variation in carbonate fault zones: A case study from the Island of Malta. Journal of Structural Geology 76, 61–79, https://doi.org/10.1016/j.jsg.2015.04.005.

Nabavi, S.T., and Fossen, H., 2021. Fold geometry and folding – a review. Earth-Science Reviews, 103-812, https://doi.org/10.1016/j.earscirev.2021.103812.

Ramsay, J. G., 1967. Folding and fracturing of rocks. Mc Graw Hill Book Company, 568.

Ramsay, J.G., 1974. Development of Chevron Folds. Bulletin of the Geological Society of America 85, 1741–1754. https://doi.org/10.1130/0016-7606(1976)87<1664:DOCFD>2.0.CO;2.

Ramsay, J.G., and Graham, R.H., 1970. Strain variation in shear belts. Canadian Journal of Earth Sciences 7, 786–813. https://doi.org/10.1139/e70-078.

Rowan, M. G., and Kligfield, R., 1992. Kinematics of large-scale asymmetric buckle folds in overthrust shear: an example from the Helvetic nappes. In Thrust tectonics 165-173. https://doi.org/10.1007/978-94-011-3066-0_14.

Ruh, J. B., Kaus, B. J., and Burg, J. P., 2012. Numerical investigation of deformation mechanics in fold- and-thrust belts: Influence of rheology of single and multiple décollements. Tectonics 31(3). http://dx.doi.org/10.1029/2011TC003047.

879 Sanderson, D. J. 1979. The transition from upright to recumbent folding in the Variscan fold belt of southwest
880 England: a model based on the kinematics of simple shear. Journal of Structural Geology 1(3), 171-180.
881 https://doi.org/10.1016/0191-8141(79)90037-3.

882 Schaltegger, U., and Brack, P., 2007. Crustal-scale magmatic systems during intracontinental strike-slip
883 tectonics: U, Pb and Hf isotopic constraints from Permian magmatic rocks of the Southern Alps.
884 International Journal of Earth Sciences 96, 1131–1151. https://doi.org/10.1007/s00531-006-0165-8.

885 Schmid, S.M., Fügenschuh, B., Kissling, E., and Schuster, R., 2004. Tectonic map and overall architecture of
886 the Alpine orogen. Eclogae Geologicae Helvetiae 97, 93–117. https://doi.org/10.1007/s00015-004-
887 1113-x.

888 Selli, L., 1998. Il lineamento della Valsugana fra Trento e Cima d'Asta: cinematica neogenica ed eredità
889 strutturali permo-mesozoiche nel quadro evolutivo del Sudalpino Orientale (NE-Italia). Memorie della
890 Società Geologica Italiana 53, 503-541.

891 Serpelloni, E., Vannucci, G., Anderlini, L., and Bennett, R.A., 2016. Kinematics, seismotectonics and seismic
892 potential of the eastern sector of the European Alps from GPS and seismic deformation data.
893 Tectonophysics 688, 157–181. https://doi.org/10.1016/j.tecto.2016.09.026.

894 Sibson, R. H., 1994. Crustal stress, faulting and fluid flow. Geological Society, London, Special Publications
895 78(1), 69-84. https://doi.org/10.1144/GSL.SP.1994.078.01.07.

896 Simpson, G.D.H., 2009. Mechanical modelling of folding versus faulting in brittle-ductile wedges. Journal of
897 Structural Geology 31, 369–381. https://doi.org/10.1016/j.jsg.2009.01.011.

898 Skjernaa, L., 1980. Rotation and deformation of randomly oriented planar and linear structures in progressive
899 simple shear. Journal of Structural Geology 2(1-2), 101-109. https://doi.org/10.1016/0191-
900 8141(80)90039-5.

901 Smith, S.A.F., Billi, A., di Toro, G., and Spiess, R., 2011. Principal Slip Zones in Limestone: Microstructural
902 Characterization and Implications for the Seismic Cycle (Tre Monti Fault, Central Apennines, Italy).
903 Pure and Applied Geophysics 168, 2365–2393. https://doi.org/10.1007/s00024-011-0267-5.

Stefani, C., Fellin, M. G., Zattin, M., Zuffa, G. G., Dalmonte, C., Mancin, N., and Zanferrari, A., 2007. Provenance and paleogeographic evolution in a multi-source foreland: The Cenozoic Venetian-Friulian Basin (NE Italy). Journal of Sedimentary Research 77(11–12), 867–887. https://doi.org/10.2110/jsr.2007.083.

Stewart, I. S., and Hancock, P. L., 1991. Scales of structural heterogeneity within neotectonic normal fault zones in the Aegean region. Journal of Structural Geology 13(2), 191-204. https://doi.org/10.1016/0191-8141(91)90066-R.

Swanson, E.M., Wernicke, B.P., Eiler, J.M., and Losh, S., 2012. Temperatures and fluids on faults based on carbonate clumped-isotope thermometry. American Journal of Science 312, 1–21, https://doi.org/10.2475/01.2012.01.

Tavani, S., Storti, F., Salvini, F., and Toscano, C., 2008. Stratigraphic versus structural control on the deformation pattern associated with the evolution of the Mt. Catria anticline, Italy. Journal of Structural Geology 30, 664–681. https://doi.org/10.1016/j.jsg.2008.01.011.

Tavani, S., Storti, F., Lacombe, O., Corradetti, A., Muñoz, J.A., and Mazzoli, S., 2015. A review of deformation pattern templates in foreland basin systems and fold-and-thrust belts: Implications for the state of stress in the frontal regions of thrust wedges. Earth-Science Reviews 141, 82–104. https://doi.org/10.1016/j.earscirev.2014.11.013.

Tavarnelli, E., 1997. Structural evolution of a foreland fold-and-thrust belt: The Umbria-Marche Apennines, Italy. Journal of Structural Geology 19, 523–534. https://doi.org/10.1016/s0191-8141(96)00093-4.

Tavarnelli, E., Mazzarini, F., Scialoja, E., and Isola, I., 2021. Deformation history of a foredeep basin during the incorporation of its deposits within an advancing orogenic wedge: The case of the Oligocene-Early Miocene Macigno Costiero Formation, southern Tuscany, northern Apennines, Italy. Journal of Structural Geology 147, 104347. https://doi.org/10.1016/j.jsg.2021.104347.

Tesei, T., Collettini, C., Viti, C., and Barchi, M.R., 2013. Fault architecture and deformation mechanisms in exhumed analogues of seismogenic carbonate-bearing thrusts. Journal of Structural Geology 55, 167–181. https://doi.org/10.1016/j.jsg.2013.07.007.

930 Tondi, E., Antonellini, M., Aydin, A., Marchegiani, L., and Cello, G., 2006. The role of deformation bands,
931 stylolites and sheared stylolites in fault development in carbonate grainstones of Majella Mountain,
932 Italy. Journal of Structural Geology 28, 376–391. https://doi.org/10.1016/j.jsg.2005.12.001.

933 Trevisani, E., 1991. Il Toarciano-Aaleniano nei settori centro-orientali della piattaforma di Trento (Prealpi
934 Venete). Rivista Italiana Di Paleontologia e Stratigrafia 97(1), 99–124.

935 Twiss, R.J. and Moores, E.M., 1992. Structural Geology. W.H. Freeman and Company, New York, 532.

936 Vignaroli, G., Viola, G., Diamanti, R., Zuccari, C., Garofalo, P. S., Bonini, S., and Selli, L., 2020. Multistage
937 strain localisation and fluid-assisted cataclasis in carbonate rocks during the seismic cycle: Insights from
938 the Belluno Thrust (eastern Southern Alps, Italy). Journal of Structural Geology 141, 104216.
939 https://doi.org/10.1016/j.jsg.2020.104216.

940 Whitaker, A. E., & Bartholomew, M. J., 1999. Layer parallel shortening; a mechanism for determining
941 deformation timing at the junction of the Central and Southern Appalachians. American Journal of
942 Science 299(3), 238-254. https://doi.org/10.2475/ajs.299.3.238.

943 Wieczorek, J., 1988. Maiolica - a unique facies of the western Tethys. Annales Societatis Geologorum Poloniae
944 58, 255–276.

945 Winterer, E.L., and Bosellini, A., 1981. Subsidence and sedimentation on Jurassic passive continental margin,
946 southern Alps, Italy. American Association of Petroleum Geologists Bulletin 65, 394–421,
947 https://doi.org/10.1306/2f9197e2-16ce-11d7-8645000102c1865d.

948 Zuccari, C., Vignaroli, G., and Viola, G., 2021. Geological map of the San Donato–Costa Thrust Zone, Belluno
949 Thrust System, eastern Southern Alps (northern Italy). Journal of Maps 17(2), 337-347.
950 http://dx.doi.org/10.1080/17445647.2021.1946444.

951

952

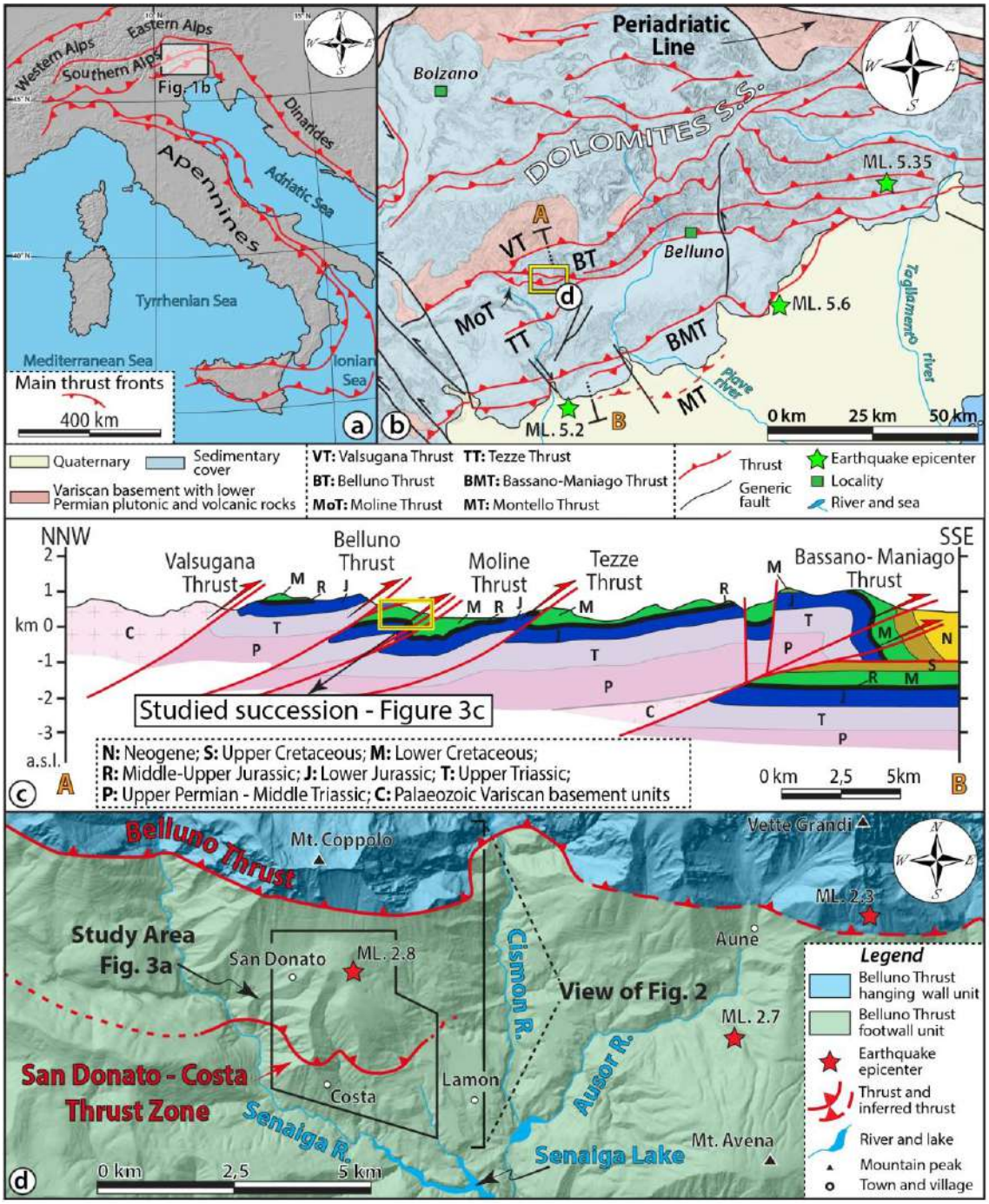

Fig. 1. a) Schematic tectonic framework of Italy showing the main thrust fronts. b) Simplified geological-structural map of the Eastern Southern Alps (ESA) southern sector in the Belluno Thrust (BT) area (redrawn and modified after Castellarin & Cantelli, 2000 and Doglioni, 1990); shown earthquake epicentres are the three of the most destructive events of the ESA (Galadini et al., 2005). c) Representative geological cross-section across the ESA (redrawn and modified after Selli, 1998; Bosellini et al., 2003; Doglioni & Carminati, 2008). The trace of the geological section is shown in (b). d) Simplified geological map of the area encompassing the Belluno Thrust (BT) and the San Donato-Costa Thrust Zone (modified from Zuccari et al., 2021). The location of the study area is indicated. The epicentres of the three most recent earthquakes (ISIDe database) affecting the study area since 1985 are reported.

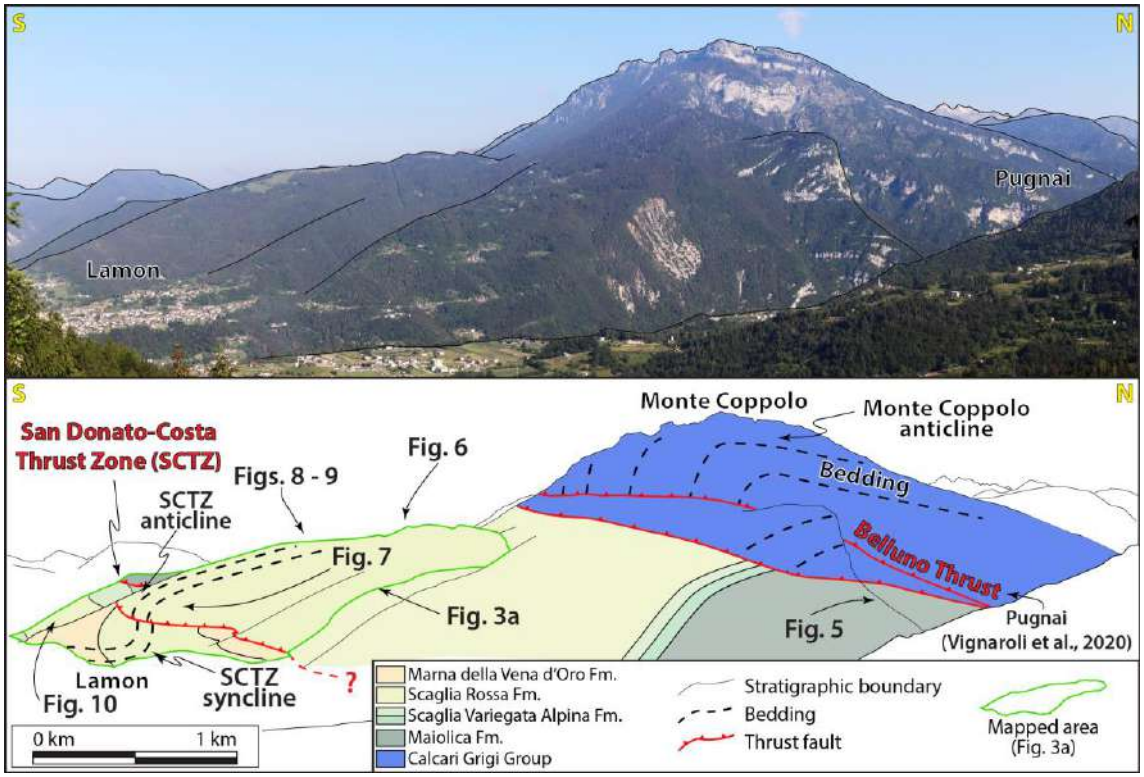

Fig 2. Panoramic view of part of the study area showing the San Donato-Costa Thrust Zone dissecting the footwall succession of the Belluno Thrust. Note the bedding attitude deformed by thrust-related anticlines and synclines.

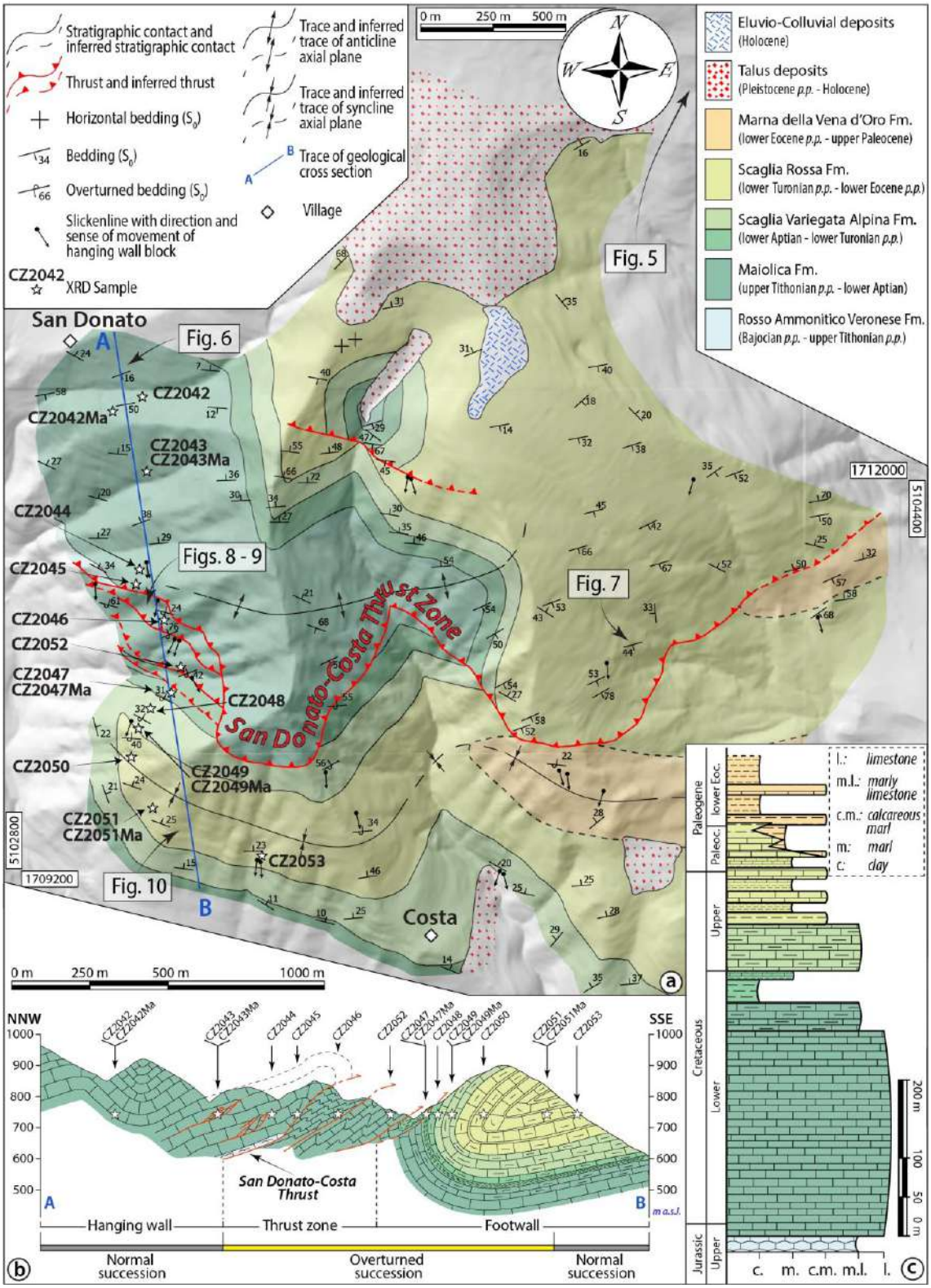

Fig. 3. a) Geological map of the San Donato-Costa Thrust Zone (after Zuccari et al., 2021). b) Representative geological cross-section across the thrust. c) Stratigraphic and lithological column of the sedimentary multilayer succession deformed by the thrust. Locations of XRD samples shown in (a) and (b). l.: limestone; m.l.: marly limestone; c.m.: calcareous marl; m.: marl; c.:clay.

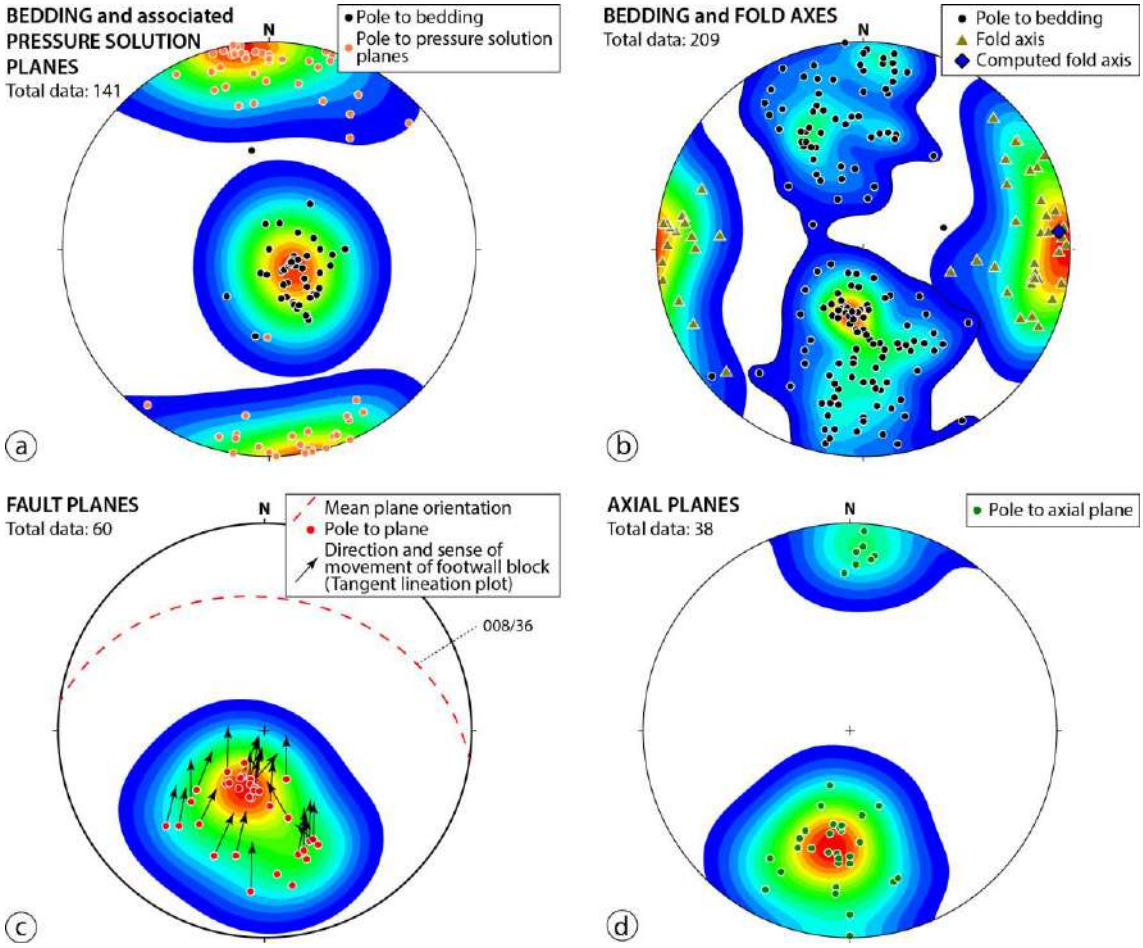

Fig. 4. Lower hemisphere stereographic projections (Schmidt net) of measured structural elements. a) Contours of poles to bedding and poles to pressure solution planes of the northern portion of the hanging wall domain. b) Contour of poles to bedding, fold axes and computed fold axis ("Bingham Analysis" on pole to bedding). c) Contour of poles to fault planes with tangent lineation data displaying the direction and sense of movement of fault footwall blocks. d) Contour of poles to axial planes. Kamb contour values: interval = 1, Significance level = 2 (Kamb, 1959).

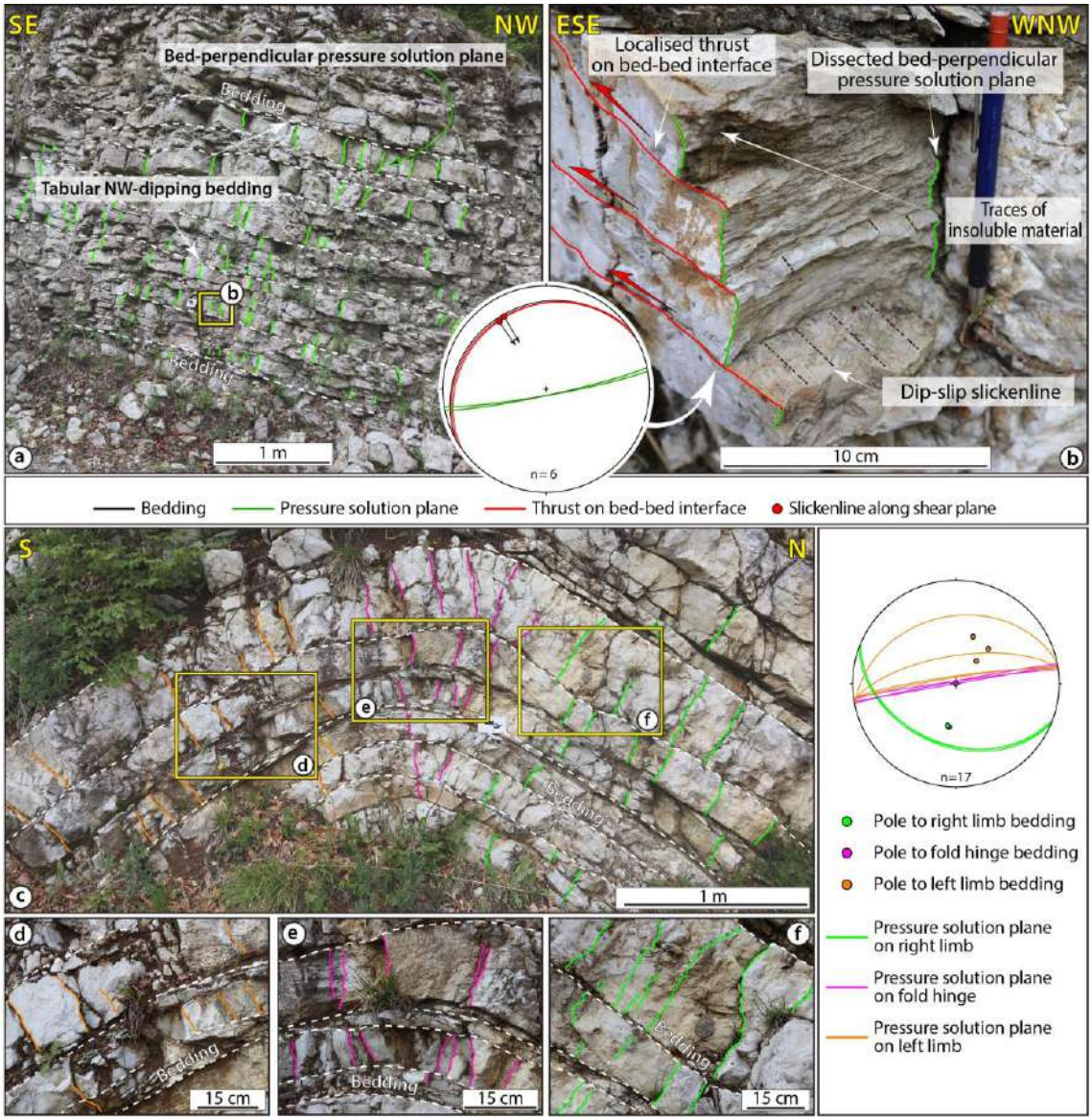

Fig. 5. Pressure-solution planes within the Maiolica Fm. in the northern hanging wall domain of the SCTZ. a) Tabular NW-dipping succession with pervasive bed-perpendicular pressure solution planes. b) Bedding parallel thrust surfaces dissecting the pressure solution planes. c) WNW-trending open buckle fold characterised by pervasive bed-perpendicular pressure-solution planes. d) N-dipping pressure solution planes on S-dipping limb. e) Sub-vertical pressure solution planes in fold hinge. f) S-dipping pressure solution planes on the N-dipping limb. Colours of structural elements in (a) and (f) are consistent with those reported in the Schmidt nets (lower hemisphere projection).

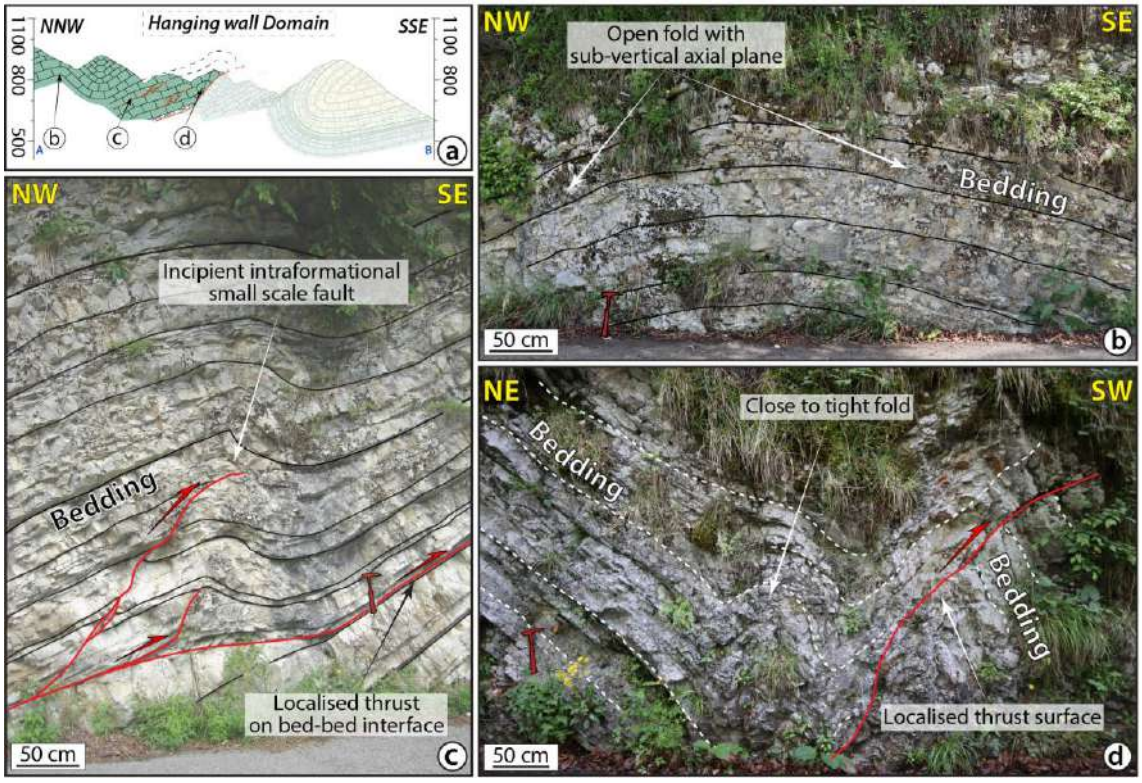

Fig. 6. Deformation structures within the Maiolica limestone in the SCTZ hanging wall domain. a) Location of studied outcrops along the SCTZ section. b) Open upright fold with metric wavelength and amplitude. c) Folds with wavelength of ~ 90 cm and amplitude of ~ 40 cm. Low-displacement top-to-the SE reverse faults cut across the folded sequence. d) Close to tight fold near the SCTZ.

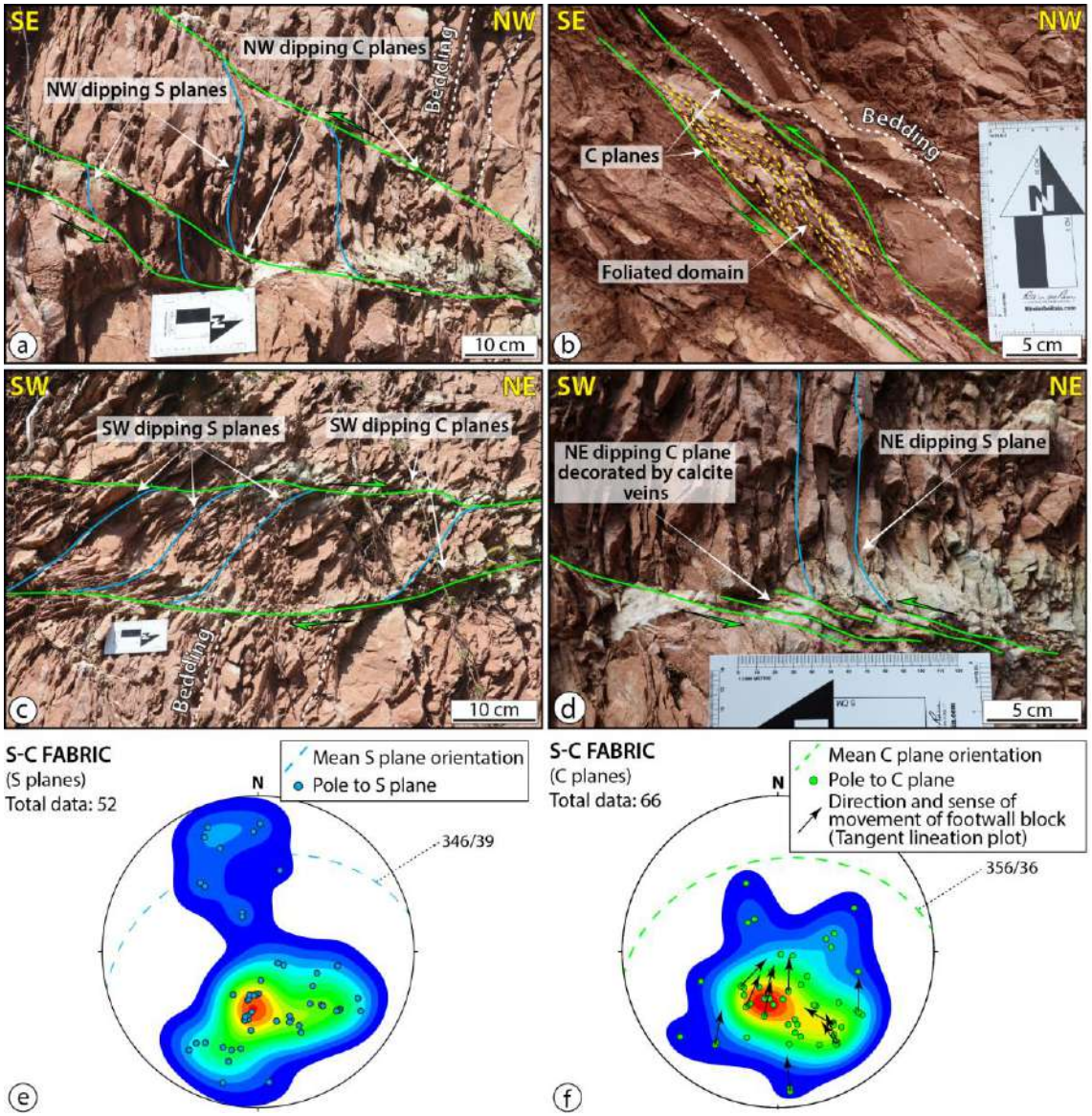

Fig. 7. Deformation structures within the eastern sector of the SCTZ hanging wall domain. a) S-C fabric deforming the sub-vertical forelimb within the more marly portion of the Scaglia Rossa Fm. b) Foliated domain with S-C fabric in marly interlayers parallel to bedding on gently dipping fold back limb within the Scaglia Rossa Fm. c) Top-to-the NE S-C fabric within the calcareous portion of the Scaglia Rossa Fm. d) Detail of C planes decorated by calcite veins bounded by slip surfaces. e) Contours of poles to S planes; mean S plane orientation shown by dashed great circle. f) Contours of poles to C planes; mean C plane orientation shown by dashed green great circle. Lower hemisphere Schmidt net projections. Kamb contour values: interval = 1, Significance level = 2 (Kamb, 1959).

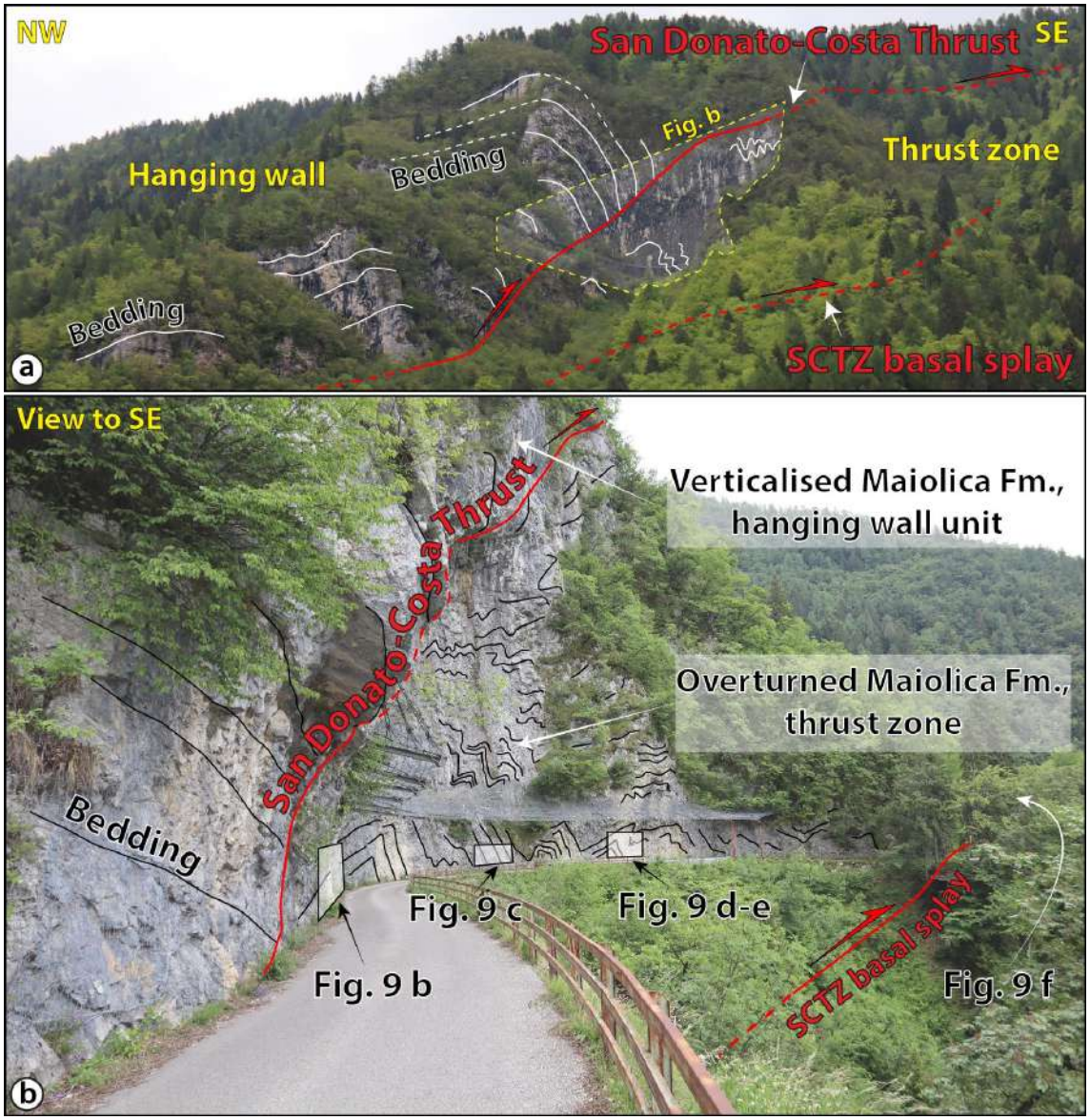

Fig. 8. Panoramic view of the San Donato-Costa Thrust zone (SCTZ). a) Panoramic view of the main hanging wall anticline of the SCTZ. Note the difference in folding style between hanging wall and footwall. b) Detailed view of the SCTZ footwall containing asymmetric and faulted folds within the overturned Maiolica Fm.

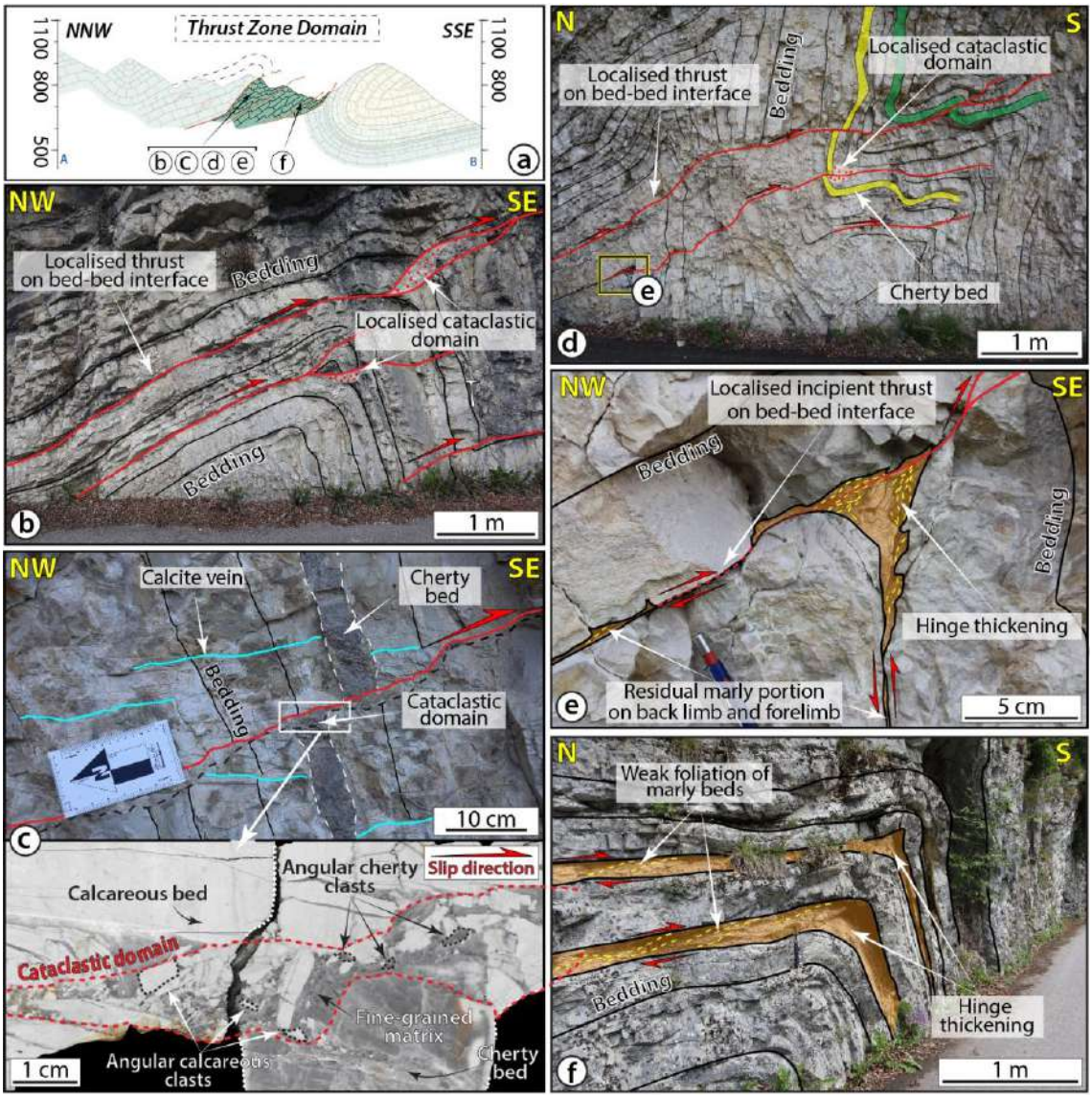

Fig. 9. Deformation structures within the thrust zone domain. a) Location of the studied outcrops. b) Asymmetric and SE-verging fold with multiple reverse faults cutting through the verticalized forelimb (note the associated cataclasite). c) Localised cataclastic domain along the verticalized beds of the Maiolica Fm. (top) and detail of the polished hand specimen of the cataclastic domain, composed of mixed calcareous and cherty clasts (bottom). d) Multiple reverse faults with centimetric offset cutting through the verticalized forelimb of a S-verging anticline. e) Foliated marls in hinge thickened by marl flow during progressive folding. f) Asymmetric and SE-verging fold and marly interbeds deformed in response to flexural slip and layer-parallel shearing (LPS) during progressive folding.

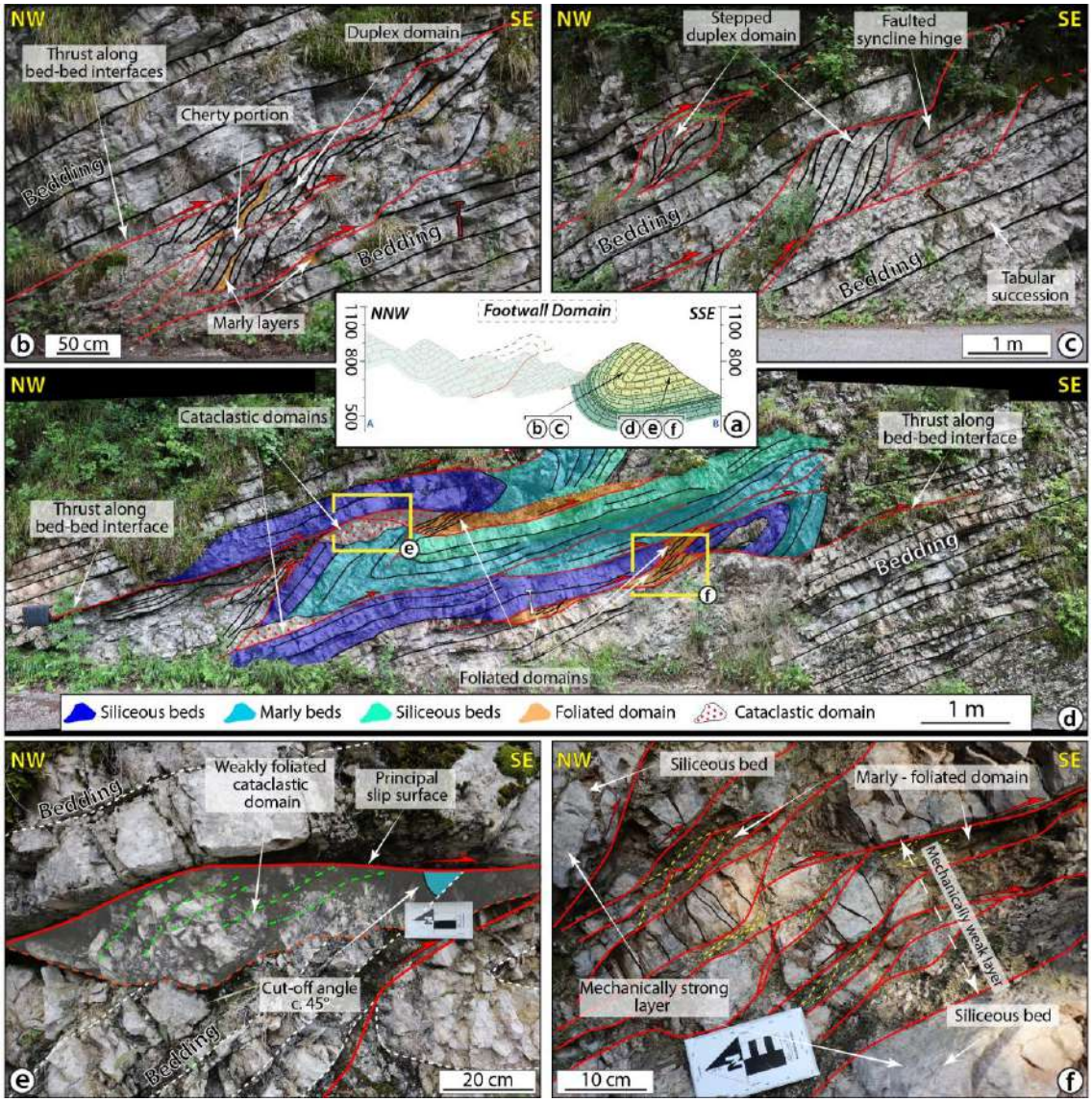

Fig. 10. a) Location of the studied outcrops; b) Marly beds transposed along horses within duplex domain. c) Duplex domain within the steeply dipping syncline back limb. d) m-scale duplex structures defined by N-dipping and top-to-the SE floor and roof thrusts. Centimetric to decimetric asymmetric lithons of siliceous and marly beds embedded within pervasively foliated marly beds. e) Incipient cataclastic domain with oblique foliation concordant with top-to-the S sense of shear. f) Foliated domain with multiple sigmoidal calcareous lithons attesting to top-to-the SE sense of shear.

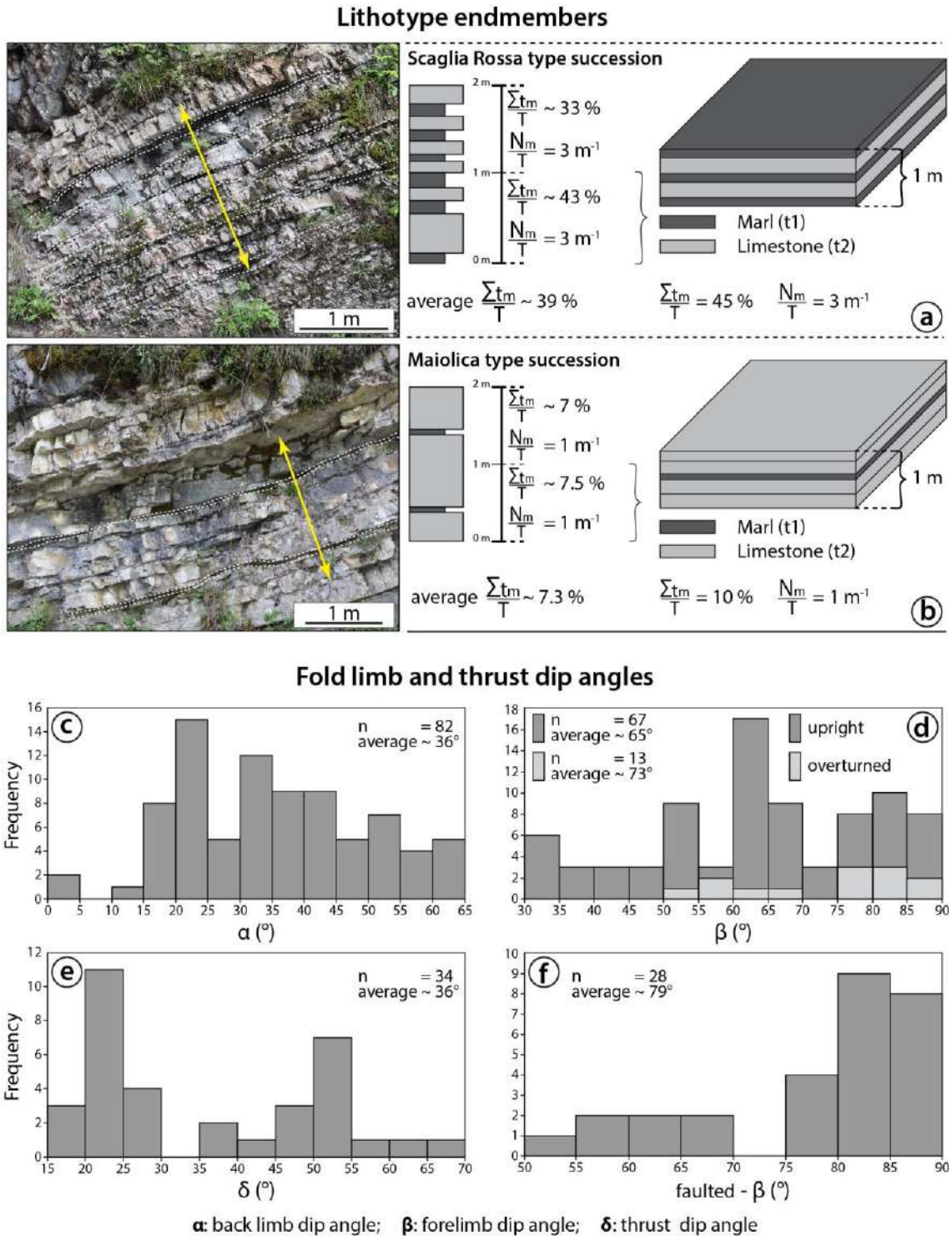

Fig. 11. Definition of the endmember lithotypes and of the geometrical relationships between back limb, forelimb and thrust surface dip angle. a) and b) Field analogue and conceptualisation of the Scaglia Rossa and Maiolica endmembers, respectively, reporting the thickness of marly and calcareous beds with respect to the reference measured succession. c) Readings of back limb dip angles (α). d) Readings of forelimb dip angles (β). e) Reading of thrust fault dip angles (δ). f) Readings of forelimb dip angles of limbs cut by thrust faults. Data are from 82 folds and 34 thrusts from the study area. $\sum t_m/T$: ratio between the cumulative thickness of marly layers and the total thickness of the measured succession; N_m/T: ratio between the number of marly layers and the total thickness of the measured succession.

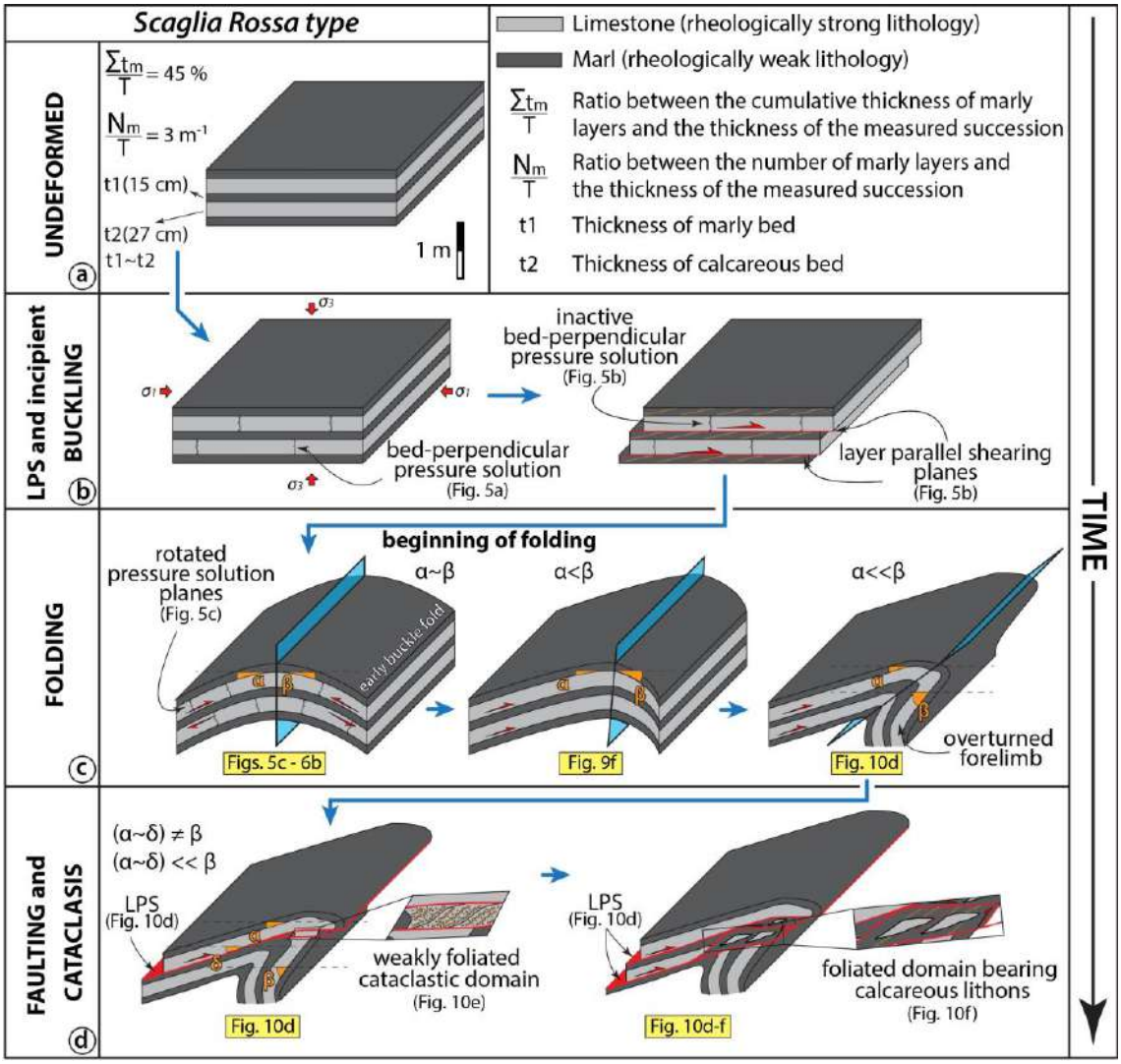

Fig. 12. Deformation model for the Scaglia Rossa endmember. a) The starting condition represents the middle portion of the Scaglia Rossa Fm. in the study area, with $\sum t_m/T$ = 45% and N_m/T =3 m^{-1}. b) Layer parallel shortening, layer parallel shearing and incipient buckling stage, showing the bed-perpendicular pressure solution planes and the transition to the progressive shearing along bed-bed interfaces. c) Folding stage showing the progressive fold evolution from symmetric to asymmetric and verging through the steepening of the forelimb. d) Faulting and cataclasis stage showing the "decapitation" of an asymmetric fold, where the thrust localises along the marly layers, and the progressive evolution and widening of the fault zone. Yellow labels refer to outcrop examples shown in the indicated figure. LPS: Layer Parallel Shearing.

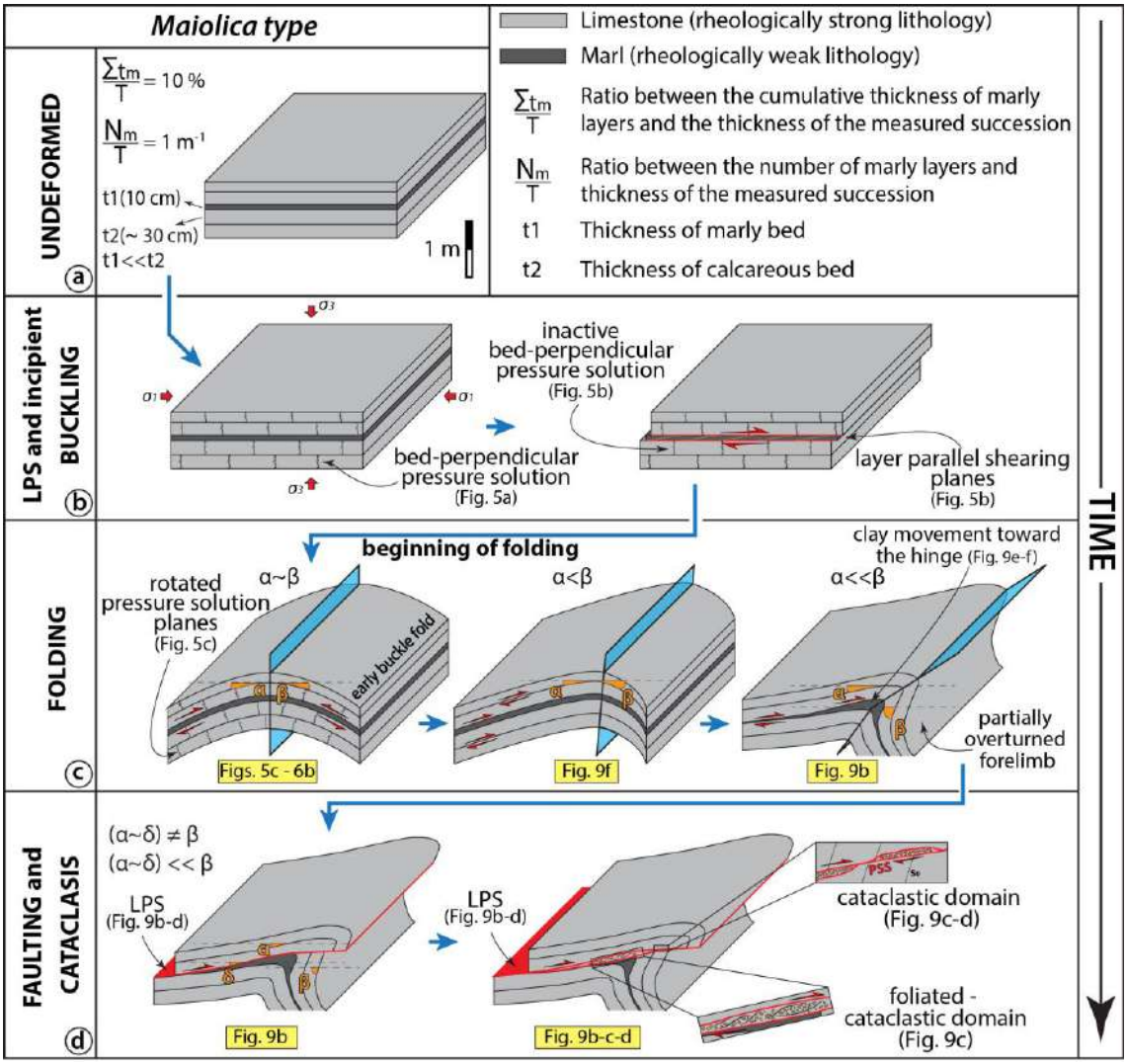

Fig. 13. Deformation model for the Maiolica endmember. a) The starting condition represents the middle and most calcareous portion of the Maiolica Fm. in the study area, with $\sum t_m/T = 10$ % and $N_m/T = 1m^{-1}$. b) Layer parallel shortening, layer parallel shearing and incipient buckling stage, showing the bed-perpendicular pressure solution planes and the progressive evolution into shear along bed-bed interfaces exploiting the only one marly layer. c) Folding stage showing the progressive evolution of fold, starting from the symmetric early buckle fold, with the passive rotation of bed-perpendicular pressure solution planes, from symmetric to asymmetric geometry, related to the continuous steepening of forelimb. d) Faulting and cataclasis stage showing the development of a discrete thrust that localises along one single marly layer and "decapitation" of the asymmetric fold. The second part of this stage shows the evolution and widening of the fault zone by also considering the involved rock type (marly vs. calcareous). Yellow labels refer to outcrop examples shown in the indicated figure. LPS: Layer Parallel Shearing.

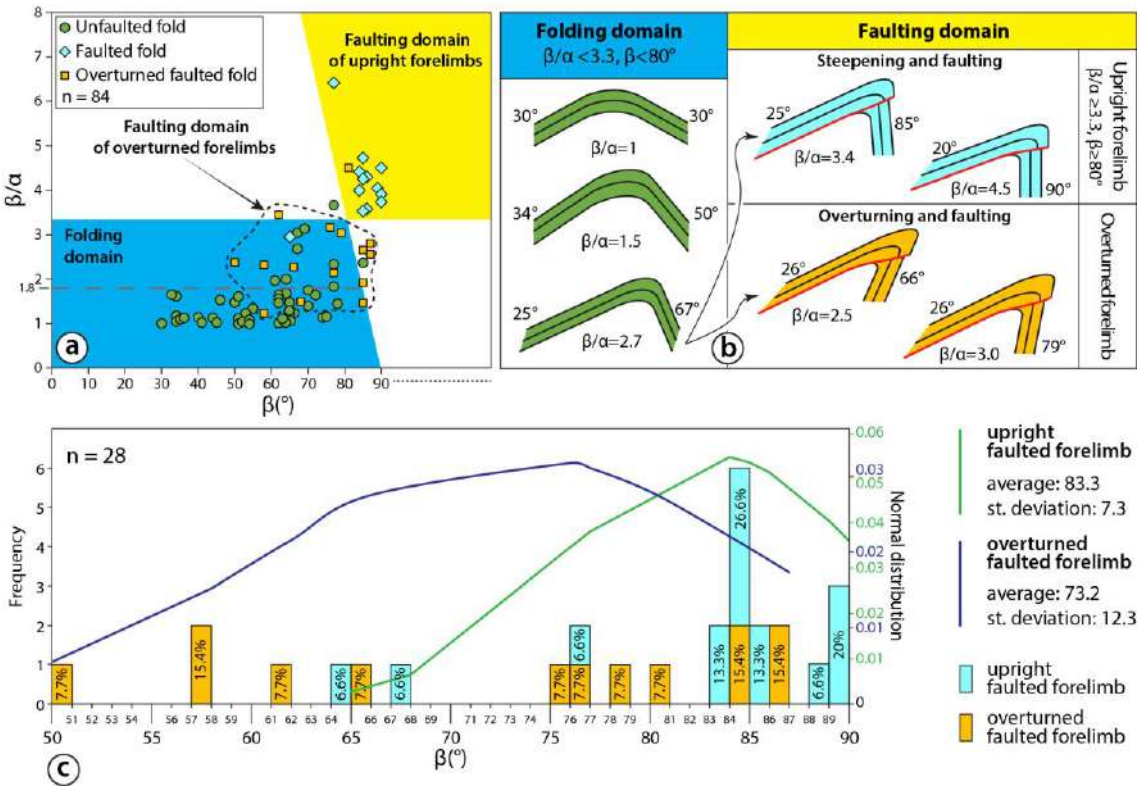

Fig. 14. Quantification of the critical angle from folding to faulting. a) Fields of stability of different deformation mechanisms as a function of the variation of the fold limb dip angle. b) Conceptualisation of back limb and forelimb geometry during folding. c) Frequency of forelimb dip angle of faulted folds and normal data distribution.

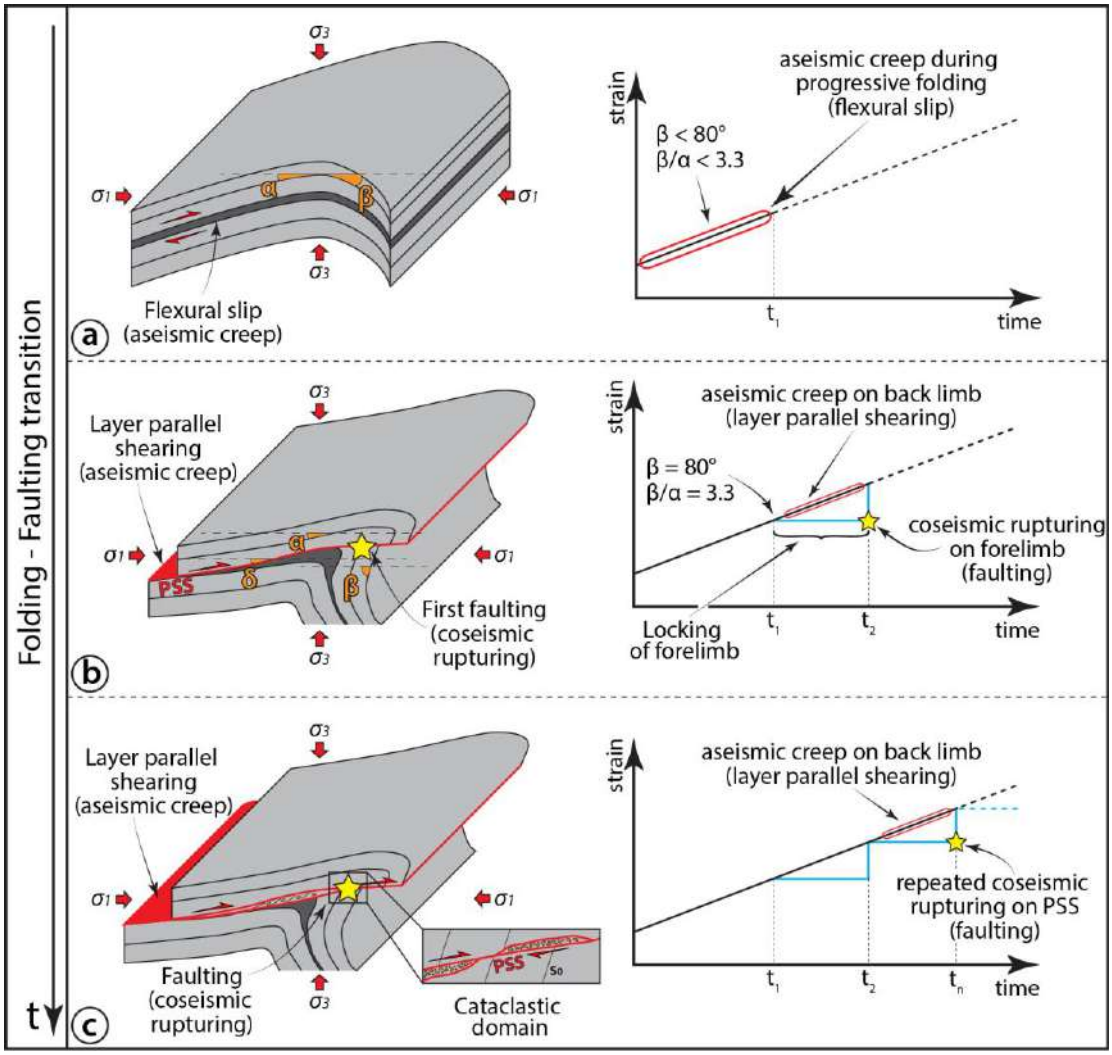

Fig. 15. Conceptual model of strain localisation during the folding-faulting transition and related aseismic vs seismic behaviour. a) Folding stage, where flexural slip develops aseismically along bed-bed interfaces ($\beta < 80°$ and $\beta/\alpha < 3.3$). b) First stage of faulting after the fold-locking stage (t1, $\beta = 80°$ and $\beta/\alpha = 3.3$): layer parallel shearing deforms the back limb, exploiting bed-bed interfaces, in an aseismic regime, whereas simultaneous seismic faulting dissects the forelimb (t2) with localised slip and fracturing. c) Evolved faulting (t_n) inducing repeated seismic rupturing along newly formed principal slip surfaces (PSS) during widening of the fault zone and development of the cataclastic domain, whereas aseismic deformation of the back limb acts via layer parallel shearing.